

# Beyond dual-porosity modeling for the simulation of complex flow mechanisms in shale reservoirs

Bicheng Yan<sup>1</sup> · Yuhe Wang<sup>2</sup>  · John E. Killough<sup>1</sup>

Received: 21 July 2014 / Accepted: 3 November 2015 / Published online: 27 November 2015  
© Springer International Publishing Switzerland 2015

**Abstract** The state of the art of modeling fluid flow in shale reservoirs is dominated by dual-porosity models which divide the reservoirs into matrix blocks that significantly contribute to fluid storage and fracture networks which principally control flow capacity. However, recent extensive microscopic studies reveal that there exist massive micro- and nano-pore systems in shale matrices. Because of this, the actual flow mechanisms in shale reservoirs are considerably more complex than can be simulated by the conventional dual-porosity models and Darcy's law. Therefore, a model capturing multiple pore scales and flow can provide a better understanding of the complex flow mechanisms occurring in these reservoirs. This paper presents a micro-scale multiple-porosity model for fluid flow in shale reservoirs by capturing the dynamics occurring in three porosity systems: inorganic matter, organic matter (mainly kerogen), and natural fractures. Inorganic and organic portions of shale matrix are treated as sub-blocks with different attributes, such as wettability and pore structures. In kerogen, gas desorption and diffusion are the dominant physics. Since the flow regimes are sensitive to pore size, the effects of nano-pores and micro-pores in kerogen are incorporated into the simulator. The multiple-porosity model is built upon a unique tool for simulating general multiple-porosity systems in which several porosity systems may be tied to each other through arbitrary connectivities. This new model allows us to better understand complex flow mechanisms and eventually is extended into the reservoir scale through upscaling techniques. Sensitivity studies on the

contributions of the different flow mechanisms and kerogen properties give some insight as to their importance. Results also include a comparison of the conventional dual-porosity treatment and show that significant differences in fluid distributions and dynamics are obtained with the improved multiple-porosity simulation.

**Keywords** Shale reservoir · Random distribution · Apparent permeability · Multiple porosity modeling · Upscaling

## 1 Introduction

The development of unconventional resource plays in North America has achieved great success towards satisfying the growing energy demand, with the application of horizontal well drilling and hydraulic fracturing. The organic shale formations which provide the basis of unconventional oil and gas production continue as an enigma as far as understanding production characteristics are concerned. Because of this, many investigators have been inspired to establish suitable models to characterize fluid flow in shale encountering great challenges along the way.

Shale is referred to as extraordinarily fine-grained sediments commonly showing fissility [22]. Loucks et al. [26] systematically classified nanometer- to micron-sized pores in the shale matrix into interparticle pores and intraparticle pores associated with mineral particles and organic matter pores within kerogen. The organic matter has different physical properties from common rock constituents and significantly affects gas storage and flow in shale. Curtis et al. [10] found that mostly kerogen is scattered in inorganic matter, and pores within it are basically round in cross section interestingly with numerous small pores residing on the

✉ Yuhe Wang  
yuhe.wang@me.com

<sup>1</sup> Texas A&M University, College Station, TX, USA

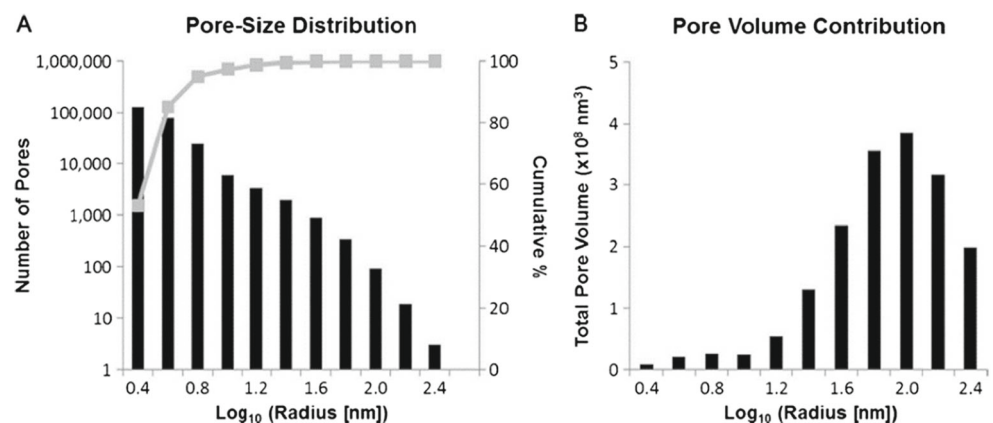
<sup>2</sup> Texas A&M University at Qatar, Doha, Qatar

interior walls of larger pores. Due to forming during the process of hydrocarbon generation, the pore networks in the organic matter in shale are mainly considered to be oil or gas wet [31, 41]. Experiments on the Barnett Shale demonstrated that both the adsorbed gas and free gas stored in the shale matrix are linearly increased with total organic carbon (TOC) content [21], and Javadpour [22] also theoretically proposed that besides free gas storage in shale, gas is also be adsorbed on the surface of kerogen and dissolved within it. Hill and Nelson [18] estimated that between 20 and 85 % of gas in shale might be stored as adsorbed gas. All those features make organic matter in shale unique and lead us to accept the proposal that the porosity systems in organic-rich shale are separated into four types: inorganic matter, organic matrix (kerogen), natural fractures, and hydraulic fractures [41].

Indeed, fracture networks provide the flow pathways to produce hydrocarbon from shale matrix, and thus, there exist different aspects of complexity in shale reservoirs, including reservoir heterogeneity (fracture and matrix) and fluid flow mechanisms in the shale matrix. To efficiently characterize fracture heterogeneity in shale, different approaches have been applied to simulate unconventional reservoirs. Wu et al. [42] proposed a useful framework to simulate unconventional gas reservoirs through a hybrid fracture modeling approach, including explicit fracture modeling, multiple interacting continua (MINC), and single-porosity modeling approaches; Ding et al. [12] presented a coupled modeling approach to simulate fractured shale reservoirs by applying a numerical dynamic skin factor from a sector model into a coarse-grid model; through transmissibility computations based on a (pseudo)-steady-state near-fracture solution, Ding et al. [13] improved the techniques for conventional coarse-grid modeling of fractured wells in terms of handling long-term well performance and transient behavior. Finally, unstructured grid (Voronoi grid) has been used to characterize variable distribution of hydraulic and natural fractures with fractal-based techniques [38, 39]. Yet, fracture characterization is not the

focus of this paper, and instead we emphasize on fluid storage and flow mechanisms in shale matrix. Due to the extremely low permeability (nano-Darcy scale) in the shale matrix, many investigators consider that Darcy flow is quite limited or even breaks down in shale with pore sizes in nanometer scale. For this reason, the feasibility of conventional dual-porosity/dual-permeability models has been suspected. Instead, the flow mechanisms in tight formations have been re-investigated and many innovative methods have been proposed: the dual-mechanism approach (Darcy flow and Fickian diffusion occur parallel in matrix) was introduced to characterize the gas flow in coal or shale formations through the dynamic gas slippage factor [8, 14]; the concept of apparent permeability considering Knudsen diffusion, slippage flow, and advection flow was first derived by Javadpour [22], and it was further applied to pore-scale modeling for shale gas [35, 36]; based on a unified Hagen-Poiseuille-type formula [5], Civan [6] and Ziarani and Aguilera [46] proposed a method to calculate apparent permeability through the flow condition function (a function of Knudsen number) and the intrinsic permeability of porous medium. The validity of this latter model for different flow regimes still requires further confirmation. However, even with this greater detail, these models may not be sufficient due to the use of an undivided shale matrix. Even with a proper connectivity between different pore systems, there still remains little understanding of this aspect [4]. On the other hand, Hudson et al. [20] did categorize the shale reservoir into organic porosity, inorganic porosity, natural fractures, and hydraulic fractures and explored several different tank models for connections between each pore system. Unfortunately, the modes to characterize the distribution of each continuum and the connections between those continua appear too regular to be realistic for shale reservoirs. Clearly, there remains a strong requirement to accurately model production from unconventional reservoirs based on detailed physics of the process and the interaction among different porosities such that modeling uncertainty is reduced.

**Fig. 1** **a** Pore size distribution estimated from the Horn River reconstruction indicating that small pores dominate in number; **b** volumetric contribution of the same pores with peak at 2.0 [11]



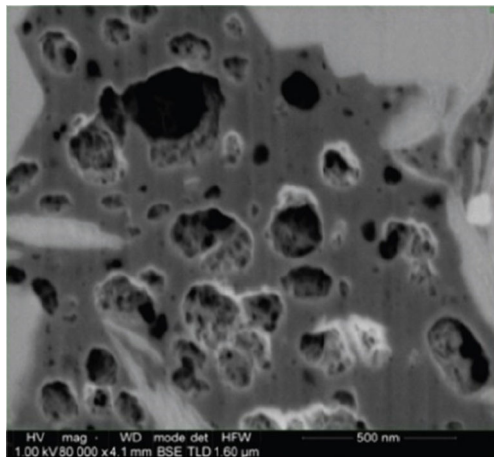


**Fig. 2** BSE image of a region of kerogen with varying pore sizes: smaller pores can be seen in the inner walls of larger pores [10]

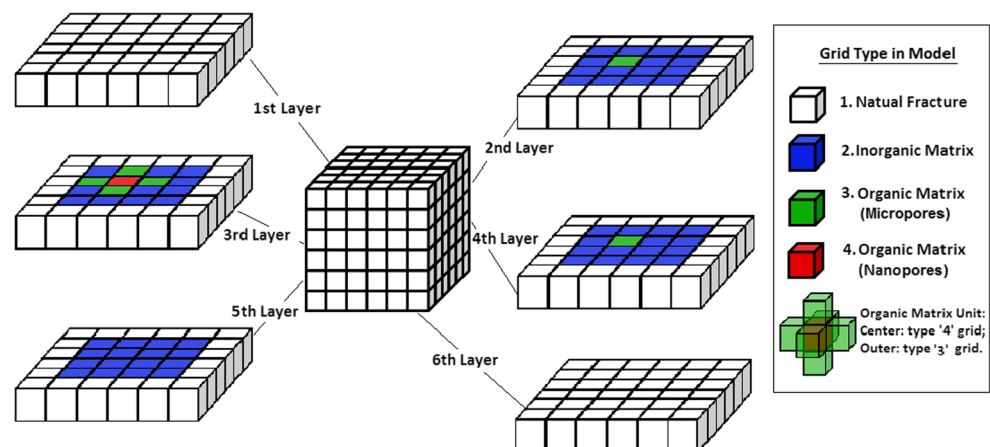
Inspired by those predecessors and relying on the wide petrophysical knowledge about shale that is available in the literature, this research considers that those conventional dual-porosity/permeability models are not sufficient to describe those complex physics and dynamics. This paper establishes a micro-scale model of shale. The scope of the micro-scale model lies between core-scale and molecular-scale. The purposes of the model are to evaluate flow mechanisms in different parts of the shale matrix in a realistic way and to ultimately upscale it for reservoir-scale simulation. Molecular-scale simulations are good choices for studying flow mechanisms and fluid properties; however, this remains an area of active research which is beyond the scope of this study. On the other hand, core-scale models with a size in the centimeter range might allow the study of important mechanisms for flow in these highly complex pore systems. The core scale is unfortunately not a good scale to observe different dynamics in the kerogen and the inorganic matrix individually, which are at most at the micron scale [3]. Therefore, as a compromise between

the different aspects above, this paper starts from a micro-scale model in the magnitude of microns to allow matrix division. This model still inherits a traditional discretization method based on continuous porous media to obtain a smooth upscaling process. Basically, the micro-scale model here features five aspects: (1) due to the importance of organic matter in shale, TOC (weight percentage of total organic carbon, wt %) is an indispensable input parameter in the model; (2) the shale matrix bulk is strictly separated into inorganic matrix and organic matrix, and to further emphasize the organic matter in shale matrix, we consider the existence of two types of porosity system distinguished in pore size in kerogen: kerogen with micro-pores and kerogen with nano-pores; (3) a well-designed algorithm which recognizes the random distribution and arbitrary connections between different continua is introduced; (4) complex mechanisms including Darcy flow, Fickian diffusion, and desorption are optionally integrated into different continua in the model; (5) finally, an upscaling approach to extend to the micro-scale model to a reservoir-scale model has been proposed. To evaluate the impact of different mechanisms on the production of shale gas, several case studies are introduced. A comparison of the micro-scale model with the conventional dual-porosity model demonstrates the differences between these two approaches. Finally, an example based on the upscaling approach demonstrates the utility of the method to ultimately extend simulations to reservoir and ultimately field scale.

## 2 Model description

With the advances in experimental conditions, such as SEM, kerogen can be characterized as generally dispersed in inorganic matter in the micron to nanometer scale. The width of natural fracture systems generally is less than 0.05 mm [24]; therefore, the simulation scale should be limited to microns at most if subdivision of shale matrix

**Fig. 3** Schematic of micro-scale model: it is a  $6 \times 6 \times 6$  grid system for instance, with one organic matrix unit randomly distributed in shale matrix core surrounded by natural fracture grid



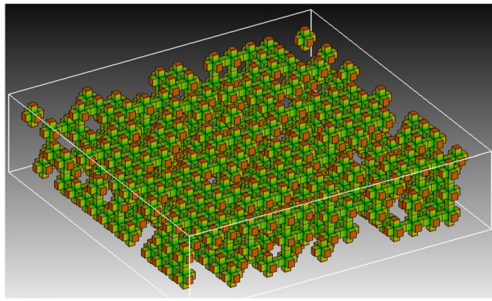


**Fig. 4** Sample micro-model with TOC = 7.0 wt% (green grids are kerogen grids)

is required. The validity of the micro-scale model work must be well-established before applying any upscaling approaches. Curtis et al. [11] stated that in the shale matrix, small pores (radii in 3 to 6 nm) predominate in the amount of pores but those larger pores (radii in 100 nm) contribute most of the pore volume as shown in Fig. 1a, b. Moreover, due to the high porosities of up to 50 % in kerogen [32] and the larger possible pore sizes in inorganic matter [26], it is necessary to further separate the organic matrix into kerogen with micro-pores (average pore radii in 100 nm) and kerogen with nano-pores (average pore radii in 5 nm). We further propose that the kerogen grids with nano-pores are only connected to the kerogen grids with micro-pores. Any other porosity systems in shale communicate with the organic matrix merely through those kerogen grids with micro-pores. This follows the observation from petrophysical data that in porous kerogen, small pores penetrate the walls of larger pores as shown in Fig. 2. Additional evidence indicates that the shale matrices are surrounded by natural fractures as pathways to connect with hydraulic fractures or the wellbore [43, 43, 45], and fractures are explicitly simulated with fine grids. Therefore, there exist four different continua in the micro-scale model:

1. Nano—kerogen grid with nano-pores with high porosity
2. Micro—kerogen grid with micro-pores with high porosity as well
3. Inorg—inorganic grid with relatively low porosity

**Table 1** Description of medium properties for the micro-scale modeling

Porosity system	Fracture	Inorganic	Kerogen	
			Micropores	Nanopores
Density (g/cc)	—	2.6	1.35	1.40
Porosity (fraction)	1.00	0.02	0.2	0.25
Permeability (mD)	84.40	$5.0 \times 10^{-5}$	$5.0 \times 10^{-5}$	0.0
Pressure (MPa)	8.6	17.2		
Temperature (K)	373.15			

4. Frac—natural fracture grid surrounding shale matrix grids to communicate with induced fractures and the wellbore.

A schematic of the mesh system is shown in Fig. 3.

Since it is assumed that kerogen grids with nano-pores can only be connected to kerogen grids with micro-pores, to realize the connectivity in space through conventional cartesian grid blocks, the smallest repeated organic matrix unit in the micro-scale model is defined as one Nano grid surrounded by six Micro grids on its six faces (Fig. 3), and thus, here the ratio of the number of Nano grids to the number of Micro grids is fixed at 1:6. To properly process the distribution of those organic matrix units in the inorganic matrix grid system, a rigorous Monte Carlo algorithm is implemented with the location of organic matrix units treated as a random parameter. In this paper, uniform size of matrix grids is used (otherwise, grid volume is required here). Therefore, providing the total number of matrix grids, TOC value, density, and porosity of different medium, then the grid number of each medium is computed through the combination of Eq. 1 and another two constrains of grid number (fixed total grid number and fixed grid number ratio of Nano grids to Micro grids):

$$\text{TOC} = \frac{\sum_{i=\text{Micro, Nano}} \rho_i N_i (1 - \varphi_i)}{\sum_{i=\text{Micro, Nano, Inorg}} \rho_i N_i (1 - \varphi_i)} \times 100\text{wt\%} \quad (1)$$

After that, the location of each organic matrix unit is randomly distributed in the inorganic grid system. This is very helpful if no realistic data of kerogen distribution in shale is available and our numerical experiments later show that this approach will bring consistent results without any bias. A sample shale matrix mesh map workable for simulation is shown in Fig. 4.

Among the four different continua listed above, gas adsorption is assumed to only occur in kerogen. Any pressure drop within the kerogen induces gas molecules to be desorbed from the kerogen surface; therefore, the gas desorption process actually increases the gas accumulation within the kerogen grid blocks in this model. This phenomenon is taken into account in the simulator used in this

**Table 2** Adsorption parameters for each case to evaluate desorption in shale (no Fickian diffusion)

Case no.	Kerogen with micropores		Kerogen with nanopores		AGWP, %
	Langmuir volume, MPa	Langmuir volume, m <sup>3</sup> /kg	Langmuir volume, MPa	Langmuir volume, m <sup>3</sup> /kg	
Case 1	0	0	0	0	0.00
Case 2	10.34	$1.0145 \times 10^{-2}$	10.34	$1.1705 \times 10^{-2}$	16.35
Case 3	10.34	$1.3266 \times 10^{-2}$	10.34	$1.4827 \times 10^{-2}$	20.28
Case 4	10.34	$1.6387 \times 10^{-2}$	10.34	$1.7948 \times 10^{-2}$	23.85
Case 5	10.34	$1.9509 \times 10^{-2}$	10.34	$2.1069 \times 10^{-2}$	27.12

work through terms of Langmuir isothermal function as Eq. 2 [7, 9, 15, 35]:

$$q_a = \rho_s \frac{M_g}{V_{std}} \frac{V_L P}{P_L + P} = \rho_s \rho_{g-std} \frac{V_L P}{P_L + P} \quad (2)$$

Because Nano grids are only connected to Micro grids as previously assumed, there are likely to be seven different connections in total, shown as following:

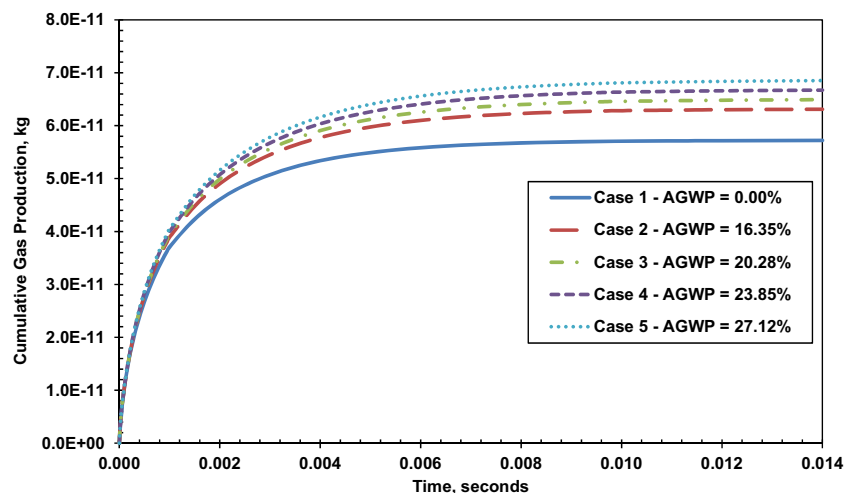
1. Micro ↔ Micro
2. Micro ↔ Nano
3. Micro ↔ Inorg
4. Micro ↔ Frac
5. Inorg ↔ Inorg
6. Inorg ↔ Frac
7. Frac ↔ Frac

In these different connections, Fickian diffusion and Darcy flow are conditionally considered based on the actual flow mechanisms. In kerogen, there are many nano-pores with small sizes very close to the size of methane molecule. Some investigators applied the Knudsen number to define the flow regimes and concluded that under such circumstances, conventional Darcy's law has been problematic [2, 23]. For that reason, we assume that free gas or desorbed

gas flows across the connection between organic matter with nano-pores and organic matter with micro-pores only through Fickian diffusion, and both Fickian diffusion and Darcy flow coexist in the connections between organic grids with micro-pores; however, there is only Darcy flow in any other connections elsewhere. From these assumptions, it follows that a general formula of the mass balance equation for a single-phase, single-component isothermal system can be written as follows (Eq. 3):

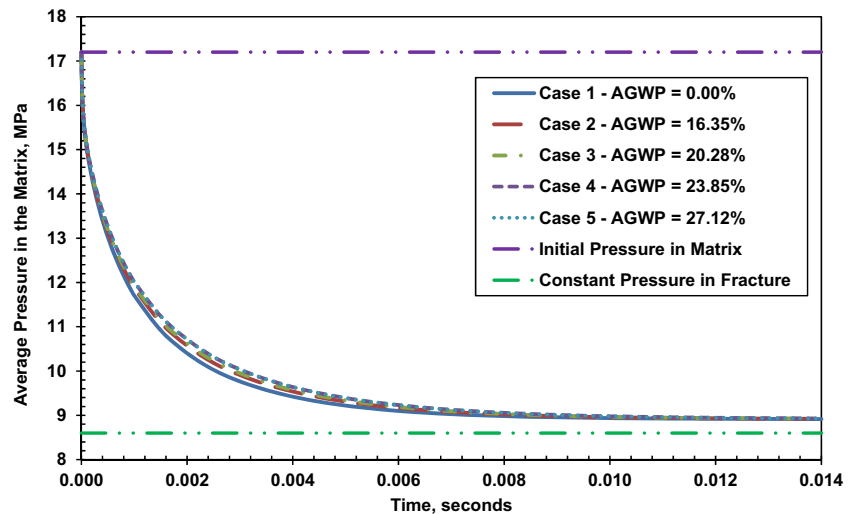
$$\nabla \cdot \left\{ \rho_g \left( D_f C_g \nabla P + \frac{K}{\mu_g} (\nabla P + \rho_g g \nabla z) \right) \right\} = - \left\{ \frac{\partial (\rho_g \varphi)}{\partial t} + \frac{\partial (q_a (1 - \varphi))}{\partial t} \right\} \quad (3)$$

The first term in Eq. 3 refers to the flux due to only Fickian diffusion, only Darcy flow, or both mechanisms acting in parallel [14]. The right hand side represents the accumulation of compressed gas in all of the grids as well as the accumulation of desorbed gas in organic grid blocks. In our simulator, Eq. 3 is solved by a fully implicit iterative algorithm. Real gas properties are computed as a function of pressure under isothermal conditions through the Peng-Robinson equation of state in the model. There are natural

**Fig. 5** Cumulative gas rate curves for five cases with different adsorbed gas weight percentages



**Fig. 6** Average pressure curves for five cases with different adsorbed gas weight percentages



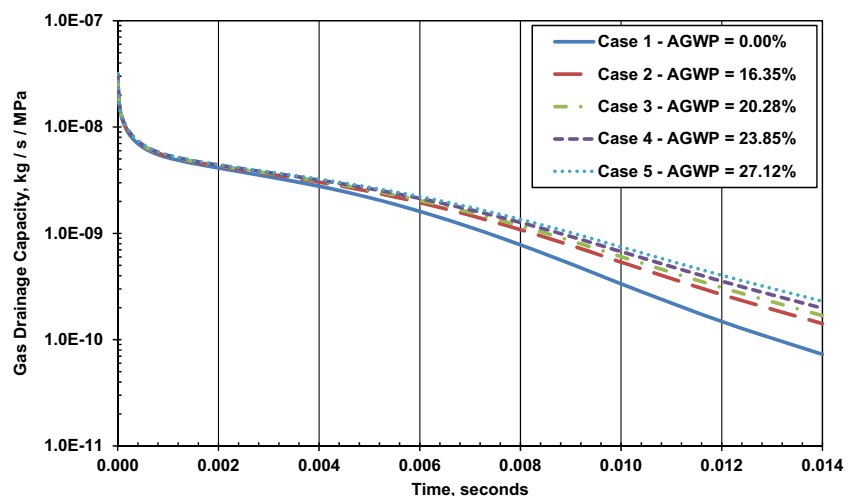
fracture grids surrounding those matrix grids and set as a constant pressure boundary for the whole system. Therefore, gas in the shale matrix will spontaneously flow into the natural fracture system until the average pressure in the matrix decreases to the same level of that in natural fracture system. Because the fracture grids are explicitly described in this model, the fracture permeability is related to fracture aperture as a cubic law [19, 33], shown in Eq. 4:

$$K_f = \frac{\delta^2}{12} \quad (4)$$

### 3 Sensitivity analysis

The dimensions of the micro-scale system are  $482 \mu\text{m} \times 482 \mu\text{m} \times 92 \mu\text{m}$  divided into 50 grids  $\times$  50 grids  $\times$  11 grids, in total 27,500 grids. Generally, the length of each matrix cub is  $10 \mu\text{m}$  and the fracture aperture is  $1 \mu\text{m}$ .

**Fig. 7** Gas drainage capacity curves for five cases with different adsorbed gas weight percentages



The TOC value is typically 12.50 wt%, and other media properties are presented in Table 1. Note that the mesh data, TOC content, and data in Table 1 are used in the following parts of this section as the default if not specified. Based on Eq. 1, the organic grid number is 5243 (the ratio of the Nano grid number to the Micro grid number is constantly 1:6). Because the gas mass within such a fine scale model is in the magnitude of  $10^{-10}$  kg, the drainage process is very short and at the later period of the drainage process the gas in place is an important constraint on gas drainage rate. Therefore, to better compare the significance of difference mechanisms on gas flow, a parameter analogous to “productivity index” is defined here, which is now called as “gas drainage capacity” (hereafter referred to as  $J_{gD}$ ),

$$J_{gD} = \frac{q_{mf}}{P_m - P_f} \quad (5)$$

Note the density of inorganic bulk and organic matter in shale is estimated from Sigal [37].

**Table 3** Diffusion coefficients for each case to evaluate Fickian diffusion in kerogen (no desorption)

Case no.	Diffusion coefficient in kerogen with micropores, m <sup>2</sup> /s	Diffusion coefficient in kerogen with nanopores, m <sup>2</sup> /s
Case 1	NA	NA
Case 2	$7.09 \times 10^{-7}$	$4.43 \times 10^{-8}$
Case 3	$7.09 \times 10^{-6}$	$4.43 \times 10^{-7}$
Case 4	$7.09 \times 10^{-5}$	$4.43 \times 10^{-6}$
Case 5	$7.09 \times 10^{-4}$	$4.43 \times 10^{-5}$

NA not available

### 3.1 Effect of desorption

To evaluate the effect of the gas desorption in kerogen on gas flow in shale, Fickian diffusion coefficients are temporarily set to zero causing Darcy flow to be the only flow mechanism. The Langmuir pressure for both Micro and Nano grids are taken as 1500 psi [20], and with different Langmuir volumes of methane in kerogen, the adsorption isotherm curve can be changed significantly causing the corresponding adsorbed gas weight percentage (hereafter referred to as AGWP) to vary. To reasonably analyze the effect of desorption, the AGWP value should be controlled within a realistic range. All parameters in Table 1 are applied here and Table 2 lists the Langmuir adsorption parameter of different organic grids for five different cases.

Figure 5 compares the cumulative gas production curves for the five cases.

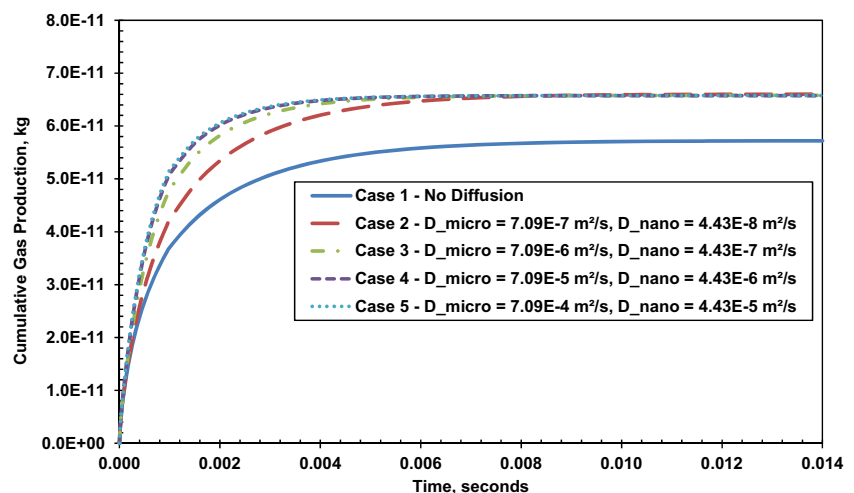
Figure 5 shows that at the early period of the gas drainage process, there is little difference among those cases because free gas in the porosity initially mainly supports the gas drainage; however, at the later period of time, the effect of desorption in kerogen becomes significant so that the cumulative gas production increases with increasing AGWP. Using case 1 without desorption as a base case, the increase

of the ultimate cumulative gas production into the natural fracture system for case 2 to case 5 is 10.3, 13.47, 16.62, and 19.77 %, respectively.

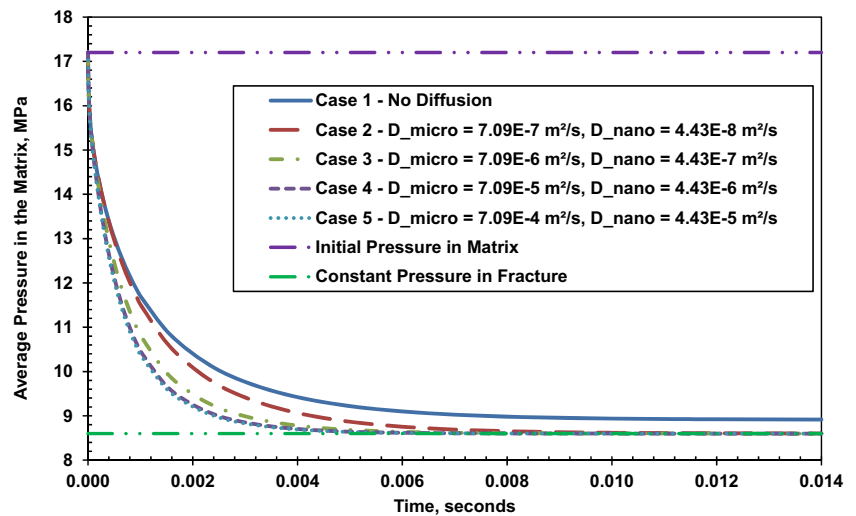
Figure 6 exhibits the change of average pressure in the matrix bulk with time. The effect of desorption helps to maintain the pressure within the matrix bulk but not substantially. It is worth noting that since in this model it is assumed that there is no Darcy flow within the organic Nano grids and with here Fickian diffusion nullified as well, the average pressure does not decline to the level in the fracture grids during the period simulated.

Figure 7 compares the curves of gas drainage capacity with time in a semi-log plot for the five cases, and through calculation, we find that during the range of 0 to 0.004 s, on average 90 % of total producible gas is drained into fracture system. Desorption only improves gas drainage capacity maximally about 16.7 % (in case 5: AGWP = 27.12 %).

Therefore, desorption increases gas drainage capacity during the later times but its influence is not considerable; the main contribution of desorption to gas flow in shale is that it increases the cumulative gas rate after pressure starts depletion. This is caused by the adsorption model applied here and the way it affects the gas flow in shale. As part of

**Fig. 8** Cumulative gas rate curves of five cases with different Fickian diffusion coefficients in kerogen

**Fig. 9** Average pressure curves for five cases with different Fickian diffusion coefficients in kerogen



accumulation term and with the same unit as gas density,  $q_a$  in Eqs. 2 and 3 should be evaluated in a time or pressure scale similar to gas density, shown in Eq. 6:

$$\frac{\partial q_a}{\partial t} = \frac{\partial}{\partial P} \left( \rho_s \rho_{g\_std} \frac{V_L P}{P_L + P} \right) \frac{\partial P}{\partial t} = \rho_s \rho_{g\_std} \frac{V_L P_L}{(P_L + P)^2} \frac{\partial P}{\partial t} \quad (6)$$

This equation implies that as pressure decreases with producing time, the effect of desorption on gas accumulation in kerogen increases significantly with given properties in the system and pressure drop.

### 3.2 Effect of Fickian diffusion

To better evaluate the effect of Fickian diffusion, the Langmuir adsorption parameters are now set to zero so that only free gas is stored in shale matrix. The mesh system and the

parameters listed in Table 1 are still used here. According to Hoteit and Firoozabadi [19], the diffusion coefficient in gas phase is in the range of  $8.7 \times 10^{-4} \text{ m}^2/\text{s}$ , so the gas diffusion coefficients of organic grids are here set in the range of  $10^{-8}$  to  $10^{-4} \text{ m}^2/\text{s}$  to conduct the sensitivity analysis. In a fashion similar to the analysis of desorption process, if the diffusion coefficient in the Nano grids is zero, gas within those grids cannot be drained out and the average pressure in the matrix cannot reach the pressure in the fracture system outside. Table 3 enumerates the Fickian diffusion coefficients in organic grids for five cases. Note that Fickian diffusion is hypothesized to only occur in kerogen.

Figure 8 shows the relationship of cumulative gas rate into the fracture system with time.

The comparison shows that there is little difference in the ultimate cumulative gas rate for those cases considering diffusion. The greater the diffusion coefficients, the faster the cumulative rate curves reach the peak level. As previously claimed, without considering diffusion, the gas stored

**Fig. 10** Gas drainage capacity curves for five cases with different Fickian diffusion coefficients in kerogen

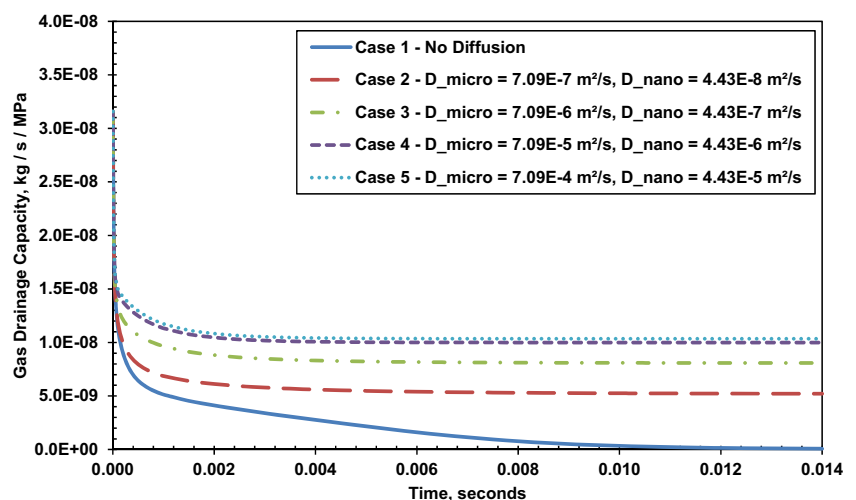




**Table 4** Parameters for dual-porosity model (no desorption)

Porosity system	Natural fractures	Shale matrix
Density (g/cc)	NA	2.20
Porosity (fraction)	1.00	0.0673
Permeability (mD)	84.40	$5.0 \times 10^{-5}$
Diffusivity ( $\text{m}^2/\text{s}$ )	NA	NA

NA not available

in Nano grids can never be produced. Comparing to the ultimate cumulative rate of cases 2 to 5, there is a significant decrease of about 15 % on average of that in case 1 (base case) which neglects diffusion in kerogen. In Fig. 9, the above observations are further confirmed: diffusion accelerates the pressure drop within the matrix bulk, and case 1 consequently maintains a little higher average pressure because of more gas left in those Nano grids.

Finally, in Fig. 10, we conclude that diffusion greatly increases the gas drainage capacity into the fracture system, especially at the later time of production or at a lower average pressure in shale matrix.

### 3.3 Comparison with dual-porosity model

With the same mesh system as above, a dual-porosity model with homogeneous matrix grids is established to compare with the micro-scale model considering Fickian diffusion and desorption, still keeping the initial pressure in matrix bulk at 17.2 MPa, pressure in fracture system constant at 8.6 MPa, and temperature in the system constant at 373.15 K. Tables 4 and 5 list the parameters related to each medium in each case.

Figure 11 shows the cumulative gas rate flowing into natural fracture system for each case. With the same gas in place, the micro-scale model only considering Fickian diffusion reaches the cumulative production plateau much earlier than the dual-porosity model and the ultimate gas recovery is almost the same.

The micro-scale model considering both Fickian diffusion and desorption has on average 12.0 % more ultimate cumulative gas rate than those of another two cases. The deviations of these three curves also indicate that Darcy flow, diffusion, and desorption occur sequentially in micro-scale model. In Fig. 12, the two micro-scale models cost almost half of the time to decrease the average pressure in the matrix bulk to the pressure in fracture system comparing to the conventional dual-porosity model, and the desorption in kerogen to some extent maintains the pressure in the matrix bulk.

Figure 13 exhibits the curves of gas drainage capacity changing with time for the three models, and it is very clear that through diffusion, the micro-scale model maintains a much greater gas drainage capacity than the dual-porosity model and desorption actually has little or even no effect to increase this parameter.

### 3.4 Effect of organic grid (kerogen) distribution in shale matrix

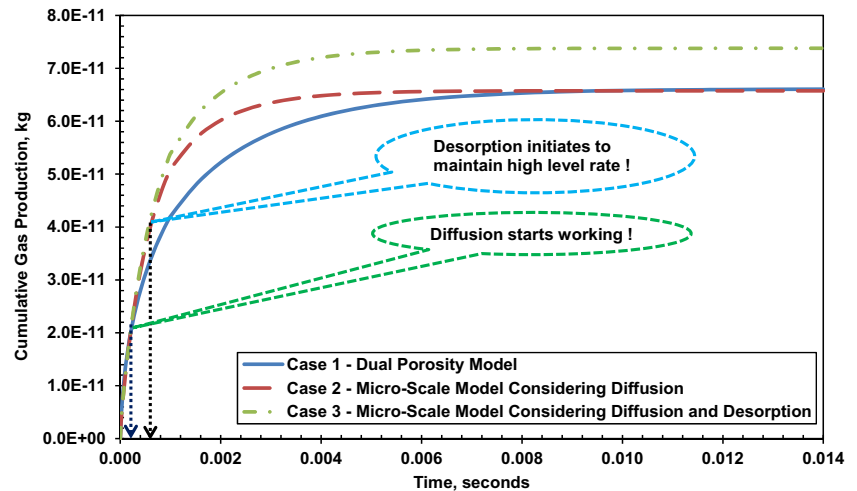
To obtain an obvious effect of random distribution for organic grids, here TOC content in shale matrix is set constant at 7.0 % (constant number of organic grids). However, the dimensions of the system are still  $482 \mu\text{m} \times 482 \mu\text{m} \times 92 \mu\text{m}$  divided into 50 grids  $\times$  50 grids  $\times$  11 grids, with fracture aperture  $1 \mu\text{m}$  and matrix cub length  $10 \mu\text{m}$ ; in the system, the temperature is constant at 373.15 K, the initial pressure in the matrix bulk is 17.2 MPa, and the pressure in

**Table 5** Parameters for the micro-scale model considering diffusion (and desorption AGWP 18.36 %)

Porosity system	Fractures	Inorganic	Kerogen	
			Micropores	Nanopores
Density (g/cc)	NA	2.60	1.35	1.40
Porosity (fraction)	1.00	0.02	0.2	0.25
Permeability (mD)	84.40	$5.0 \times 10^{-5}$	$5.0 \times 10^{-5}$	0.00
Diffusivity ( $\text{m}^2/\text{s}$ )	0.00	0.00	$7.09 \times 10^{-5}$	$4.43 \times 10^{-6}$
Langmuir pressure (MPa)	0.00	0.00	10.34	10.34
Langmuir volume ( $\text{m}^3/\text{kg}$ )	0.00	0.00	$1.1705 \times 10^{-2}$	$1.3266 \times 10^{-2}$

NA not available

**Fig. 11** Cumulative gas rate curves to compare micro-scale model with conventional dual-porosity model



natural fracture system maintains at 8.6 MPa. Other parameters related to each medium are from Table 5, but because of the lower TOC content here, the AGWP is now decreased to about 15.8 %. Five mesh systems (cases 1 to 5) with different kerogen random distribution (different random locations of organic matrix unit) are generated and coupled into the simulator.

Figure 14 shows the cumulative gas rates into the natural fracture system for the five cases; we observe that those five curves are completely overlapped with the difference between the five cases in the plot of only 0.19 %. For the results of the average pressure in the matrix bulk and the gas drainage capacity, the differences of those cases are 0.0252 and 0.3 %, respectively, and they are not plotted here for redundancy.

Therefore, the difference caused by different random kerogen distribution can be negligible here, and thus, it is concluded that the random distribution modes of kerogen

with a given TOC value do not impact the global gas flow behavior in shale.

Figure 15 is a sample matrix grid map in each layer for case 1 in Fig. 14. The organic grids (white grids) are randomly distributed within the inorganic grids (black grids), and in space, it is like a cluster of kerogen evenly distributed within the inorganic matter (Fig. 4).

Moreover, a pressure map for the matrix bulk corresponding to this mesh map is shown in Fig. 16. Through comparison of the two maps, we find that the pressure map perfectly matches with the distribution of organic grids, and in the pressure maps of four-, five-, and six-layer matrices, which are actually the inner part of the matrix bulk in a 3-D view, the pressure within organic grids (shallow red) are on average lower than that of inorganic grids (dark red) because of the well-developed and connected kerogen system compared to inorganic matter nearby. However, in pressure maps of other layer matrices which are the outer

**Fig. 12** Average pressure curves to compare micro-scale model with conventional dual-porosity model

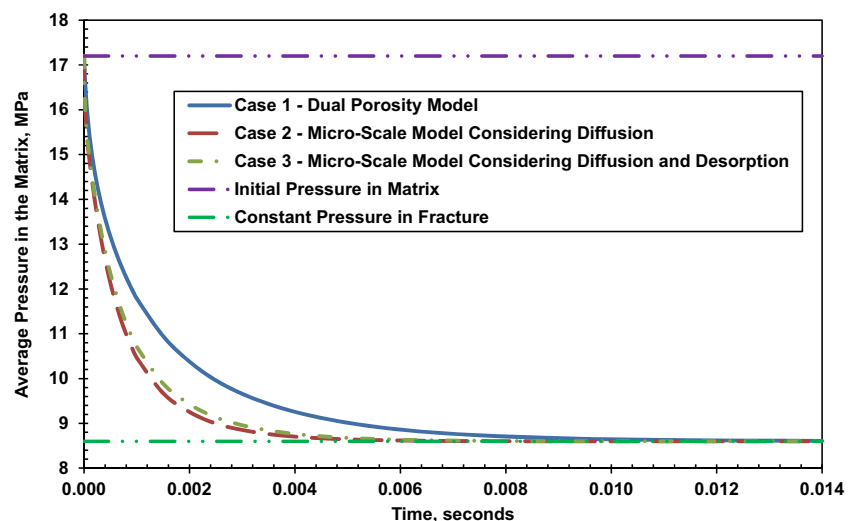
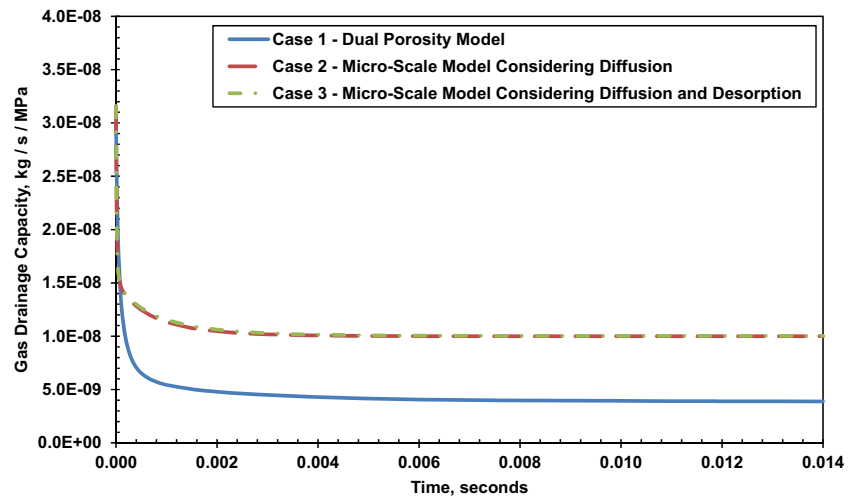


**Fig. 13** Gas drainage capacity curves to compare micro-scale model with conventional dual-porosity model



part the shale matrix, the pressure in organic grids is much higher than that in inorganic grids, and here we consider that it is partly because of the desorption effect in kerogen and partly because of the poor connectivity of kerogen at the tail end of the kerogen cluster compared to that of the inner organic grids.

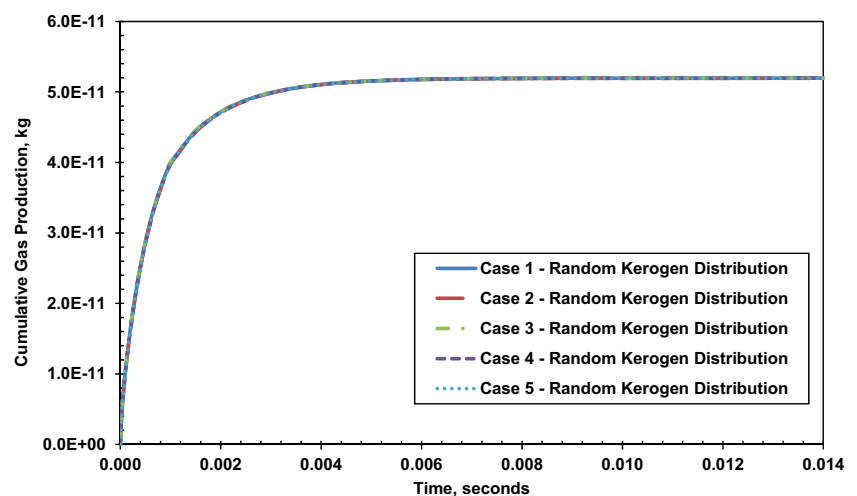
### 3.5 Effect of TOC content in shale matrix

Here we use typical TOC values 3.00 wt% (case 1), 6.00 wt% (case 2), and 12.00 wt% (case 3) to show the difference of simulation results. Still we keep the dimensions of the system  $482 \mu\text{m} \times 482 \mu\text{m} \times 92 \mu\text{m}$  divided into  $50 \text{ grids} \times 50 \text{ grids} \times 11 \text{ grids}$ , with fracture aperture  $1 \mu\text{m}$ , and matrix cub length  $10 \mu\text{m}$ ; in the system, the temperature is constant at 373.15 K, the initial pressure in the matrix bulk is 17.2 MPa and the pressure in natural fracture system maintains at 8.6 MPa. Besides, the parameters

in Table 5 for each medium are still applied. Under the initial condition in the system, the AGWP in shale matrix are respectively 11.09, 15.00, and 18.21 % for the three cases with an increase trend in TOC content.

Figures 17, 18, and 19 show the curves of the cumulative gas rate, average pressure within the matrix bulk, and gas drainage capacity into the fracture system versus time for cases 1 to 3 here. From those curves, we observe that higher TOC content in shale matrix leads to greater ultimate cumulative gas production, lower speed to decrease the average pressure in matrix bulk, and significantly higher gas drainage capacity. Kerogen has considerable gas adsorption capacity and much higher porosity than that of inorganic matter. In consequence, an increase in TOC directly brings more gas in place to sustain higher gas drainage rate. Case 2 (6.00 wt% TOC) and case 3 (12.0 wt% TOC) respectively ultimately release 1.4 and 2.1 times more gas into the fracture system than case 1 (3.00 wt% TOC). Meanwhile, because of greater gas in place for cases with higher

**Fig. 14** Cumulative gas rate curves for five cases with different kerogen distribution modes



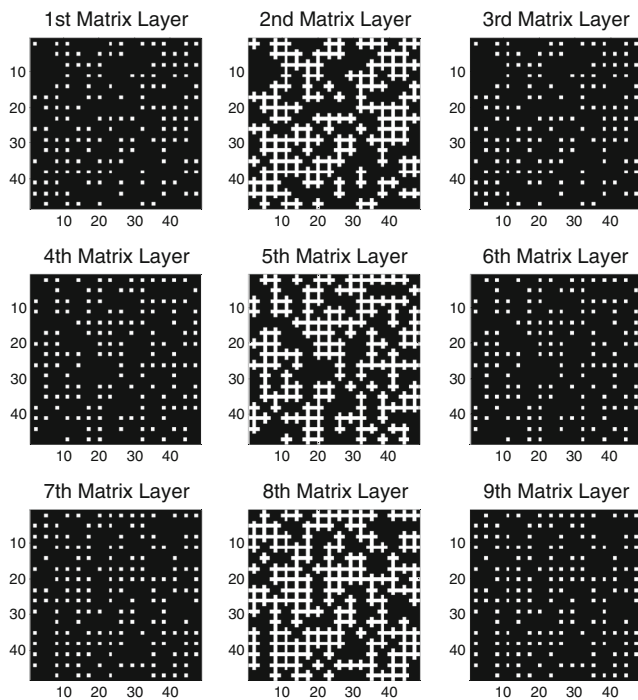
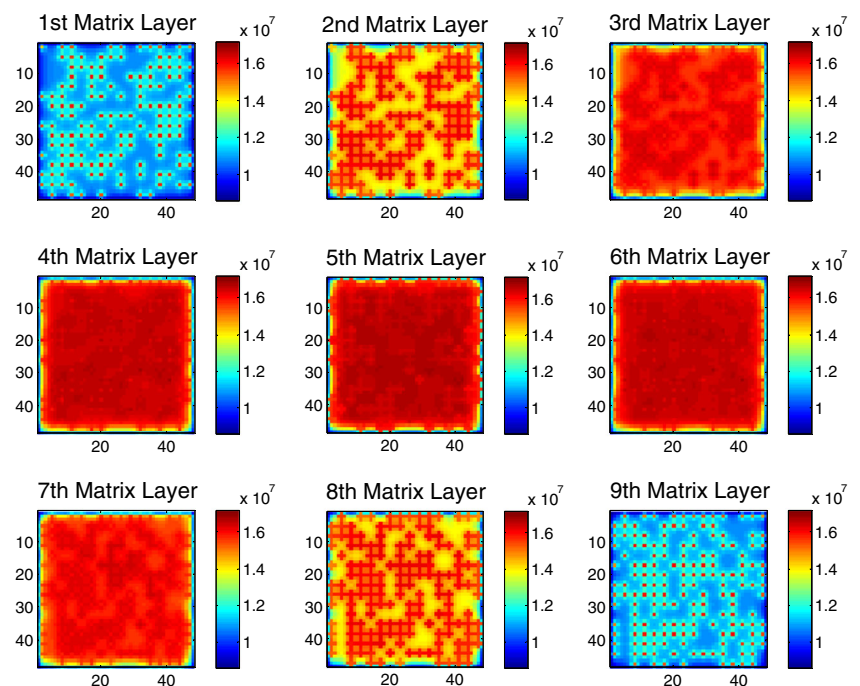


**Fig. 15** Matrix grids map distribution for nine layers of matrix in case 1 with a TOC value 7.0 %. Note that in vertical direction there are 11 layers of grids with the fracture grids contacted to the six outer faces of matrix bulk and fracture grids are not exhibited in this map

TOC content, to keep mass conservative, the average pressure in matrix bulk stays a little higher (Fig. 18). Moreover, Fickian diffusion only occurs in the organic matrix. Thus, an increase in TOC value will magnify the gas drainage

**Fig. 16** Pressure map for nine layers of matrix in vertical direction in case 1 with a TOC value 7.0 %, corresponding to the matrix mesh map in Fig. 15, and the time step is  $1.0 \times 10^{-4}$  s, when it is still at an early depletion period



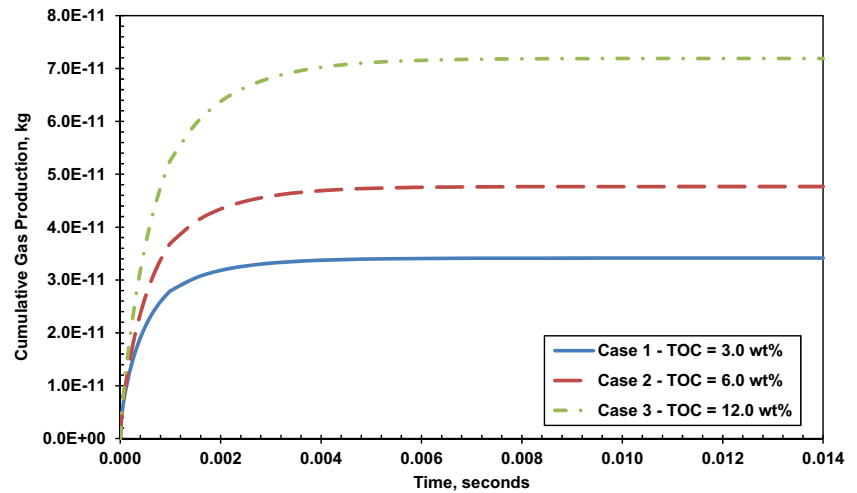
capacity due to the significantly increasing effect of Fickian diffusion in kerogen, which is exhibited in Fig. 19.

#### 4 Apparent permeability

The comprehensive work above is still limited to micro-scale simulation for qualitative analysis and obviously cannot be used for reservoir-scale simulation unless upscaling is performed. To make the work friendly to reservoir-scale simulators, an apparent permeability ( $K_{app}$ , shown in Eq. 7) is calculated for the system similar to Darcian permeability, which is now approximated as an average behavior within the matrix bulk considering the different mechanisms coupled in the model above. Meanwhile, the transient effect between matrix and fracture is also considered in Eq. 7, since the apparent permeability is calculated from the beginning of the production. Besides, there is a coefficient  $\omega$  to consider the interaction between matrix and fracture. In Eq. 8,  $K_{app}$  is a harmonic average concept considering the weight from both matrix and fracture, so through this equation, the impact of fracture permeability can be completely excluded even though it might have negligible influence on apparent permeability and a matrix apparent permeability can be obtained. For a better compatibility with the current simulator, a ratio of matrix apparent permeability to the matrix intrinsic permeability is used to tune the matrix-fracture transmissibility.

$$K_{app} = \omega \cdot \frac{q_{mf} d_{mf} \bar{\mu}_{mf}}{(\bar{P}_m - P_f) \bar{\rho}_{mf} \sum A_{mf}} \quad (7)$$

**Fig. 17** Cumulative gas rate curves for three cases with different TOC values



$$K_{app} = \frac{K_{mapp} \cdot K_f}{W_m K_{mapp} + W_f K_f} \quad (8)$$

## 5 Characteristics of matrix apparent permeability ratio

In this part, the geometric coefficient  $\omega$  in Eq. 7 is temporarily set to 1.0, and this will not influence the sensitivity of the matrix apparent permeability ratio. TOC content in shale matrix is set constant as 10.0 %. The dimensions of the model are divided into 26 grids  $\times$  26 grids  $\times$  26 grids, with 2877 organic grids and 17,576 grids in total. Organic grids are randomly distributed within matrix and fracture grids are encircling the matrix cubic bulk. Fracture aperture is constantly set as 1  $\mu\text{m}$ , but the size of matrix grid is varied from 10  $\mu\text{m}$  to 1 m. The initial pressure in matrix is set as 17.2 MPa, and pressure in natural fracture is 8.6 MPa, with temperature 373.15 K everywhere in the

system. Medium properties are from Table 5, but Fickian diffusion coefficients or Langmuir parameters are respectively nullified to analyze the effect of Fickian diffusion, desorption, and Darcy flow on matrix apparent permeability defined in Eqs. 7 and 8.

Three series of cases with different matrix sizes are simulated through the micro-scale model, and the results are plotted in Fig. 20. In Fig. 20, at the early period of pressure drop, the matrix apparent permeability ratio of those different cases is almost overlapped because of the domination of transient Darcy flow in the system at early time (Fig. 11); gradually, those cases considering diffusion would maintain a much higher level than the cases neglecting diffusion which finally decline to a very low level. On the other hand, desorption does not affect the matrix apparent permeability ratio at all because there is no difference between the latter two cases considering diffusion. From these results, it is also apparent that matrix size does not change the matrix apparent permeability ratio in any cases plotted here, which sets

**Fig. 18** Average pressure curves for three cases with different TOC values

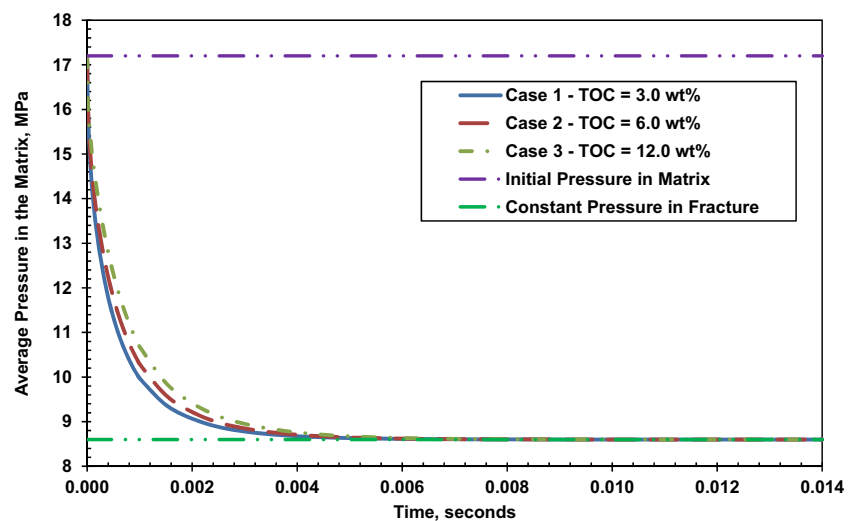
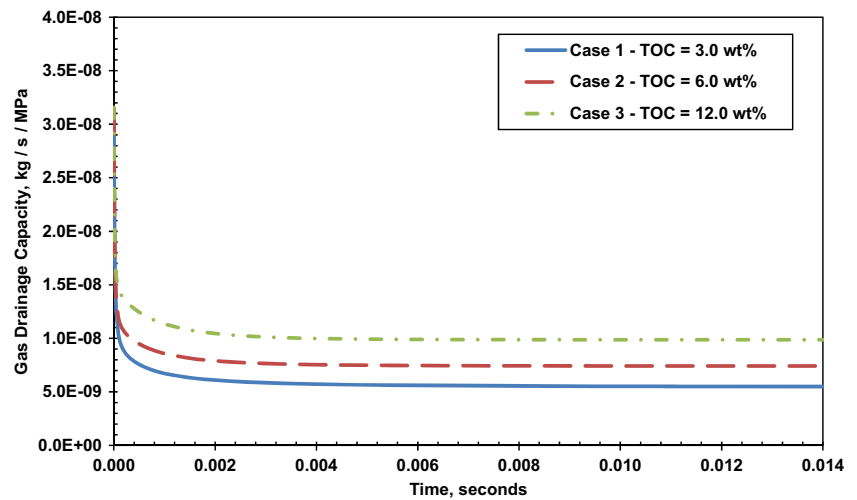




**Fig. 19** Gas drainage capacity curves for three cases with different TOC values



a solid foundation to extend the previous micro-scale model to a reservoir model later.

Based on the smallest model (matrix grid size 10  $\mu\text{m}$  and fracture grid size 1  $\mu\text{m}$ ) considering Darcy flow, Fickian diffusion, and desorption in Fig. 20, here the fracture permeability is changed from 0.844 mD to 8.44 D with any parameter else in the system the same. The result of the matrix apparent permeability ratio is shown in Fig. 21. As shown in the figure, with five fracture permeabilities in significantly different magnitudes, the curves for matrix apparent permeability ratios versus pressure have no difference and are overlapped together. Therefore, the matrix permeability ratio from Eqs. 7 and 8 is virtually an average property for the matrix including inorganic and organic grids and it has nothing to do with fracture permeability.

## 6 Matrix apparent permeability ratio with the optimum geometric coefficient - $\omega$

The sensitivity analysis above set the geometric coefficient  $\omega$  constantly at 1.0; however, the effect of upscaling under

this scenario has not yet been validated. In this part, to obtain the optimum geometric coefficient value in Eq. 7, two models are setup, including micro-scale model and bulk matrix model. Specifically, the micro-scale model with matrix extensively discretized is treated as an “accurate solution.” To validate the matrix apparent permeability ratio from this model, a bulk matrix model is established without any discretization (single matrix grid) but keeps all basic input parameters the same as the micro-scale model, and the combinational effect of Fickian diffusion and Darcy flow between matrix and fracture is considered through the matrix apparent permeability ratio. Since the matrix apparent permeability ratio has nothing to do with desorption (Fig. 20), here desorption is not considered in the micro-scale model any more. Finally, an approximate solution is obtained and further compared with the accurate solution. Through repeatedly adjusting the  $\omega$  coefficient, the approximate solution finally reaches closest to the accurate solution with an optimum  $\omega$ .

For single-component gas flow, Fickian diffusion and Darcy flow are considered to in a similar way because both of them are treated as pressure difference-related terms in

**Fig. 20** Matrix apparent permeability ratio as a function of pressure with different matrix grid sizes

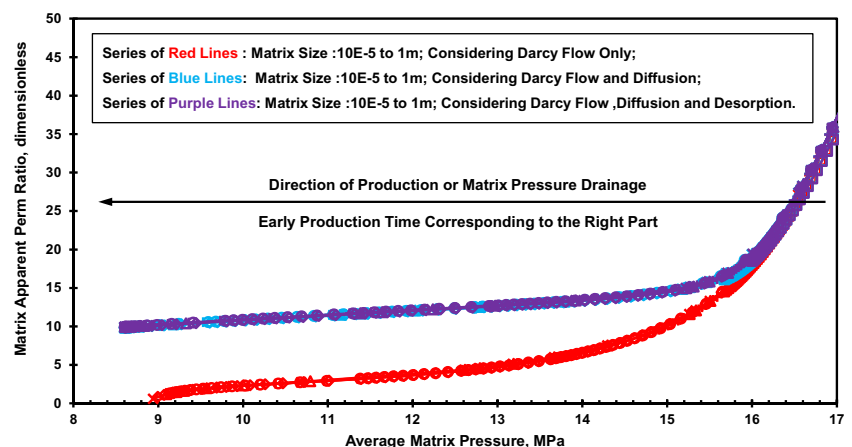
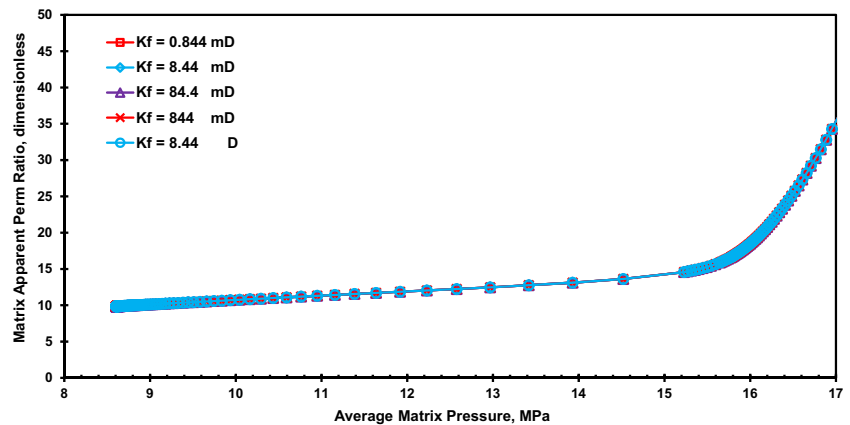


**Fig. 21** Matrix apparent permeability ratio with different fracture permeabilities



the mass balance equation for isothermal cases (Eq. 3); therefore, it is reasonable and effective to start with cases considering Darcy flow only to obtain a reasonable  $\omega$  and then apply it to cases with Darcy flow and Fickian diffusion and further validate it.

## 7 Case considering Darcy flow only

In this case, the only flow mechanism in the model is Darcy flow. The dimensions of the micro-scale model are  $242 \mu\text{m} \times 242 \mu\text{m} \times 242 \mu\text{m}$  divided into 26 grids  $\times$  26 grids  $\times$  26 grids, in total 17,576 grids (note here matrix grids are  $24 \times 24 \times 24$ ). For comparison, the dimensions of the bulk matrix model are  $242 \mu\text{m} \times 242 \mu\text{m} \times 242 \mu\text{m}$  divided into 3 grids  $\times$  3 grids  $\times$  3 grids (note here matrix grids are  $1 \times 1 \times 1$ ). The basic parameters are shown in Table 6.

It should be noted that in this case, fracture grids are single layered surrounding the matrix bulk as a constant pressure boundary.

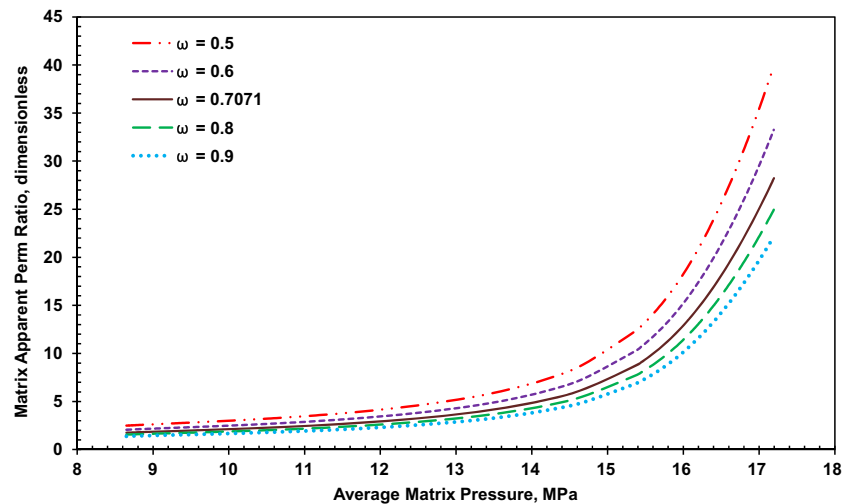
Repeated calculations were conducted to obtain an optimum value of  $\omega$  such that the difference between the

micro-scale model and the bulk matrix model is a minimum. Only five typical cases are chosen to be presented here with  $\omega = 0.5, 0.6, 0.7071$  (or  $\sqrt{2}/2$ ),  $0.8$ , and  $0.9$ , respectively. Through the micro-scale model, the dynamic matrix apparent permeability ratios are shown as Fig. 22 for different cases. With the dynamic curve applied in the bulk matrix model, the average matrix pressure and gas recovery with time are all calculated and compared with the accurate solution from the micro-scale model, shown in Figs. 23 and 24, respectively. In Fig. 23, compared to the accurate solution (case 1), the relative errors of average matrix pressure for cases 2 to 6 with different  $\omega$  values are respectively 2.52, 1.36, 1.08, 2.69, and 3.59 %. In Fig. 24, compared to the accurate solution (case 1), the relative errors of gas recovery for cases 2 to 6 with different  $\omega$  are respectively 6.02, 3.53, 2.06, 3.25, and 4.97 %. Here all those relative errors are calculated through L-2 norm. Through comparison (not only five cases shown here), the case with  $\omega = 0.7071$  (or  $\sqrt{2}/2$ ) provides the closest solution to the micro-scale model, and thus,  $\sqrt{2}/2$  is the optimum choice of  $\omega$ . The result is fairly acceptable for compressible gas flow, because the bulk matrix model reduces 70 times of the simulation time compared to the micro-scale model but

**Table 6** Basic parameters for cases considering Darcy flow only

	Micro-scale model	Bulk matrix model
$K_f$ (mD)	84.4	84.4
Fracture porosity	1.0	1.0
Fracture aperture ( $\mu\text{m}$ )	1	1
$K_m$ (nD)	50	50
Matrix porosity	0.05	0.05
Matrix grid size ( $\mu\text{m}$ )	10	10
Matrix grid no. in 3-D	$24 \times 24 \times 24$	$1 \times 1 \times 1$
Initial matrix pressure (MPa)	17.2	17.2
Pressure in fracture (MPa)	8.6	8.6
Temperature in model (K)	373.15	373.15

**Fig. 22** Matrix apparent permeability ratio from model ( $24 \times 24 \times 24$  matrix grids) considering Darcy flow only with different  $\omega$  values



without sacrificing too much accuracy. Actually the value of  $\sqrt{2}/2$  here can be explained by Furui et al. [16]; through finite element modeling the inflow of horizontal well, their results showed that the radii of radial flow region in wellbore vicinity is  $\sqrt{2}/2$  times of the boundary geometry (reservoir height). Similarly, here in the micro-scale model, matrix is bounded by fracture and radial or quasi-radial flow also occurs in fluid transfer between matrix and fracture, and thus the coefficient  $\sqrt{2}/2$  is still valid here.

## 8 Case considering Darcy flow and Fickian diffusion

Previously, we have shown that in the micro-scale model, those kerogen grids are actually evenly distributed within matrix and different random distributions of kerogen grids

with a constant TOC content cannot influence the global behavior of matrix-fracture interaction. Moreover, Fickian diffusion is similar to Darcy flow. Therefore, the method to calculate the matrix apparent permeability ratio in the case considering only Darcy flow is postulated to be also applicable to the case considering Darcy flow and Fickian diffusion; the only point neglected here is the desorption in kerogen, which has already been proven to be not related to apparent permeability previously (Fig. 20).

In this case, TOC content is controlled at 10.0 wt%, and the dimensions of the micro-scale model are still  $242 \mu\text{m} \times 242 \mu\text{m} \times 242 \mu\text{m}$  divided into  $26 \text{ grids} \times 26 \text{ grids} \times 26 \text{ grids}$ , in total 17,576 grids. For comparison, the dimensions of the bulk matrix model are  $242 \mu\text{m} \times 242 \mu\text{m} \times 242 \mu\text{m}$  divided into  $3 \text{ grids} \times 3 \text{ grids} \times 3 \text{ grids}$ . In the micro-scale model, four different continua are included while in the bulk matrix model there are only two porosity types. The parameters for the micro-scale model here are the same as those

**Fig. 23** Average matrix pressure comparison for case considering Darcy flow only with different  $\omega$  values

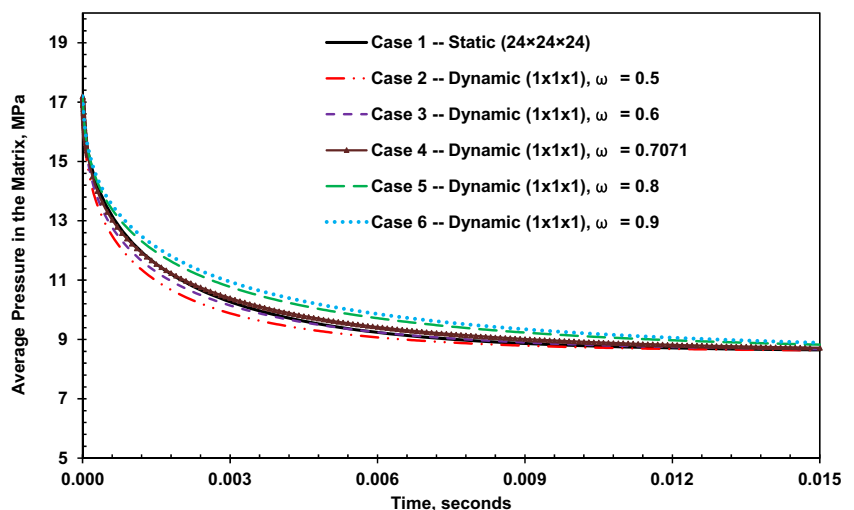
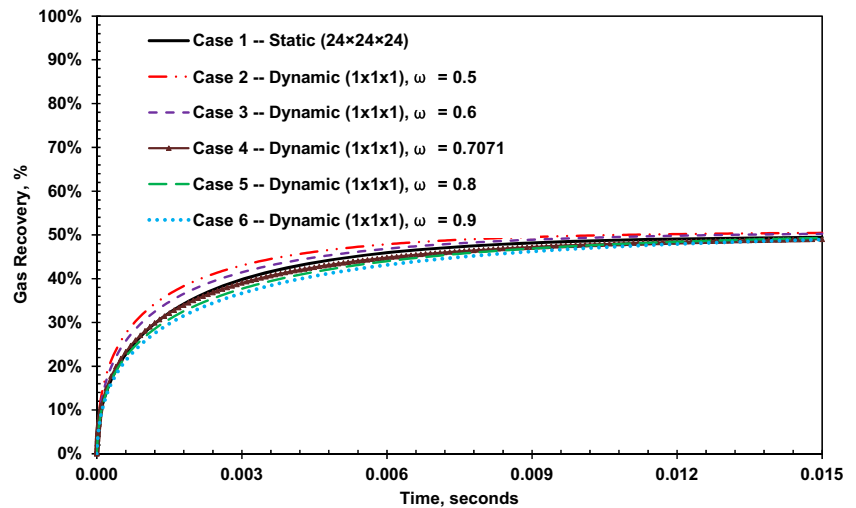
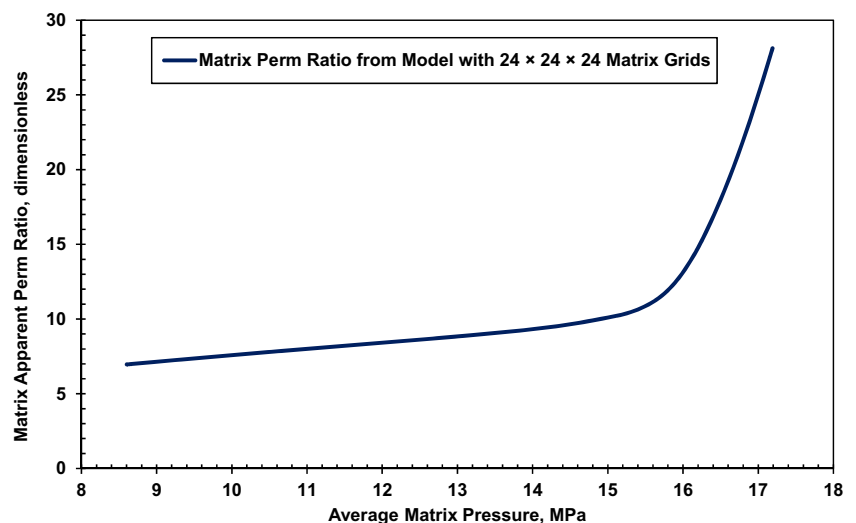


**Fig. 24** Gas recovery comparison for case considering Darcy flow only with different  $\omega$  values



in Table 5 except no desorption considered here, and those of the bulk matrix model here are the same as the parameters of the Bulk Matrix Model shown in Table 6 except its porosity averaged at 0.05895 to keep the same matrix pore volume between the two models. Based on the results from the micro-scale model, the dynamic apparent permeability is calculated with  $\omega$  equal to  $\sqrt{2}/2$ , and the matrix apparent permeability ratio is plotted in Fig. 25. The curve is further assigned as a tuning coefficient to the shale matrix permeability in the bulk matrix model. Finally, the results of these two different models in terms of dimensionless variables are plotted in Fig. 26. Compared to the micro-scale model, the relative errors of the bulk matrix model with regard to average matrix pressure and gas recovery are separately 1.4072 and 3.5693 %, which should be very good results. Therefore, the upscaled matrix apparent permeability ratio is able to accurately capture the coupled effect of different flow mechanisms and transient flow between matrix and fracture.

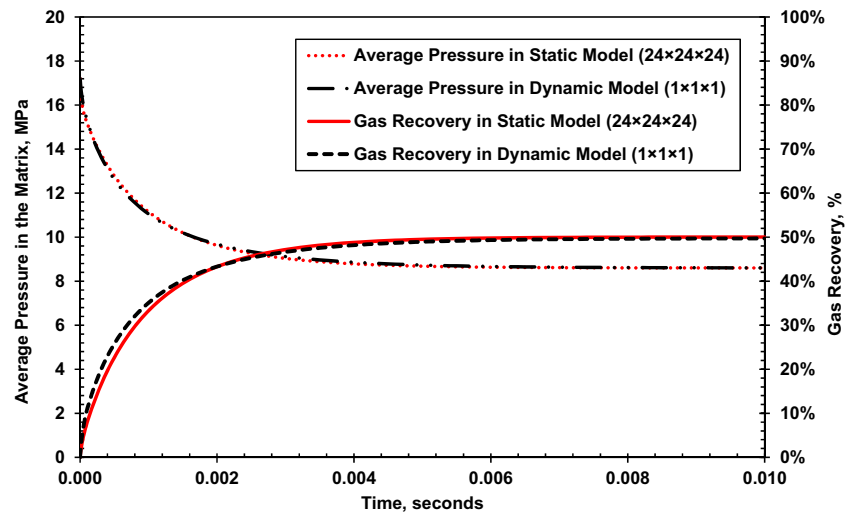
**Fig. 25** Matrix apparent permeability ratio from model considering Darcy flow and Fickian diffusion



## 9 Macro-scale modeling through dual-porosity models

After the validation of the matrix apparent permeability ratio, reservoir-scale or macro-scale modeling are now conducted through dual-porosity modeling. Different dynamic apparent permeability curves were applied to the matrix domain to consider different assumptions of physics occurrence, including dynamic apparent permeability considering Darcy flow only ( $\omega = \sqrt{2}/2$  in Fig. 22), dynamic apparent permeability considering Darcy flow and Fickian diffusion (Fig. 25), and dynamic apparent permeability ratio considering Knudsen diffusion and slippage effect based on Javadpour's model [22] for its comprehensive physical consideration. Here some important details are introduced for Javadpour's model after Swami's modification for cases of real gas and porous medium [40]. The Knudsen diffusion constant in micro- or nano-capillary is computed through

**Fig. 26** Comparison results for case considering Darcy flow and Fickian diffusion



Eq. 9, and to scale up to Knudsen diffusion constant occurring in porous media, matrix porosity and tortuosity are considered in Eq. 10. Based on real gas properties, slippage factors  $F$  is calculated through Eq. 11, and eventually all those terms feed into the calculation of apparent permeability ratio considering Knudsen diffusion and slippage flow in Eq. 12. Besides, a correlation proposed by Aguilera [1] is used to calculate average pore radii in shale matrix here, shown as Eq. 13.

$$D_k = \frac{2r}{3} \sqrt{\frac{8RT}{\pi M_g}} \quad (9)$$

$$D_m = \frac{\varphi}{\tau} D_k \quad (10)$$

$$F = 1 + \left( \frac{8\pi RT}{M_g} \right)^{0.5} \frac{\mu_g}{\bar{P} \cdot r} \left( \frac{2}{f} - 1 \right) \quad (11)$$

$$\frac{K_{Ja}}{K} = \frac{D_m C_g \mu_g}{K} + F \quad (12)$$

$$r = 2.665 \cdot \left( \frac{K}{\varphi} \right)^{0.45} \quad (13)$$

The basic parameters for macro-scale dual-porosity model are shown in Table 7.

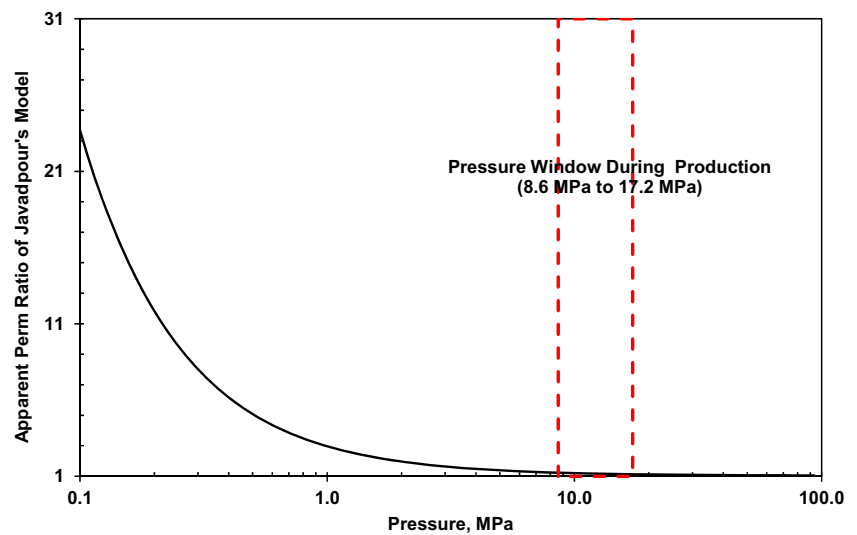
Based on the matrix properties and reservoir condition, the apparent permeability ratio of Javadpour's model is calculated (average pore radii is 19.5 nm based on Eq. 13) and plotted as Fig. 27. This is quite similar to Javadpour's result for pore radii = 10 nm (Fig. 28). In both Figs. 27 and 28, the result ratio is sensitive to pressure, especially at lower values. However, in Fig. 27 Javadpour's apparent permeability ratio is approximately 1.2 on average in the pressure drainage window of our case, and thus it does not influence the pressure drainage in matrix significantly. To keep good consistency during comparison in macro-scale models, Fig. 27 is further applied into a fine micro-scale model to interpolate matrix permeability, and through the same calculation process to get Figs. 22 and 25 (still  $\omega = \sqrt{2}/2$ ), an upscaled apparent permeability ratio curve of

**Table 7** Basic parameters for macro-scale dual-porosity model

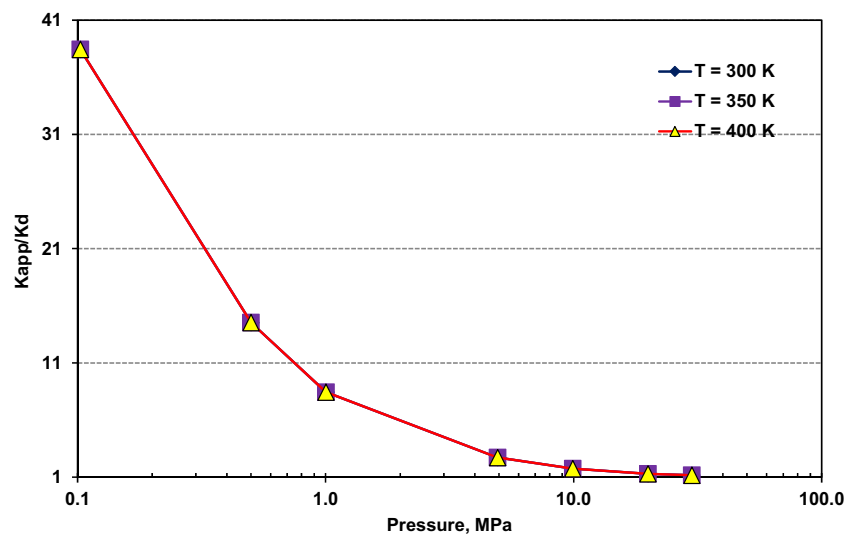
	Macro-scale model
$K_f$	84.4 mD
Fracture porosity	1.0E−3
Fracture aperture	1 $\mu$ m
$K_m$	50 nD
Matrix porosity	0.058947483
Initial matrix pressure	17.2 MPa (2494 psia)
Bottom hole pressure	8.6 MPa (1247 psia)
Temperature in model	373.15 K
Grid dimension (X-Y-Z)	10 × 10 × 1 (equal grid sizes)
Reservoir length in x-direction	304.8 m (1000 ft)
Reservoir length in y-direction	304.8 m (1000 ft)
Reservoir thickness in z-direction	30.48 m (100 ft)



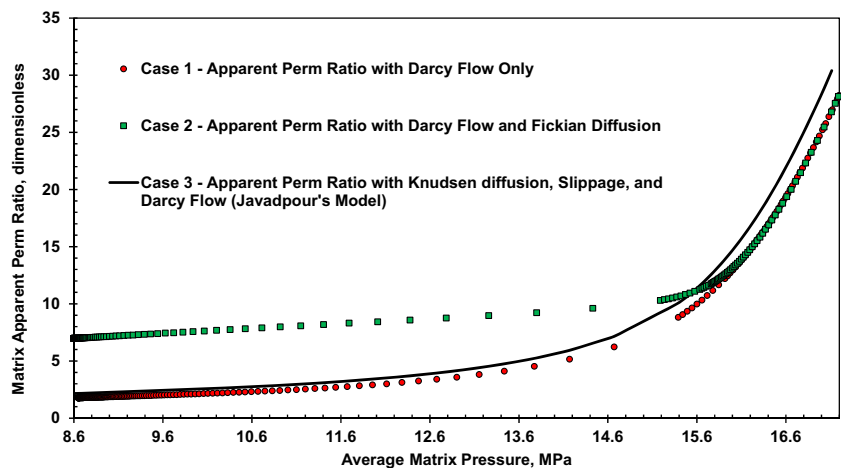
**Fig. 27** Effect of pressure on apparent permeability ratio based on data from Table 7; calculated pore radii = 19.5 nm,  $T = 373.15$  K



**Fig. 28** Effect of pressure and temperature on apparent permeability ratio with pore radii = 10 nm, reproduced after Javadpour [22]



**Fig. 29** Comparison of upscaled apparent permeability for different assumptions of flow mechanisms in shale matrix



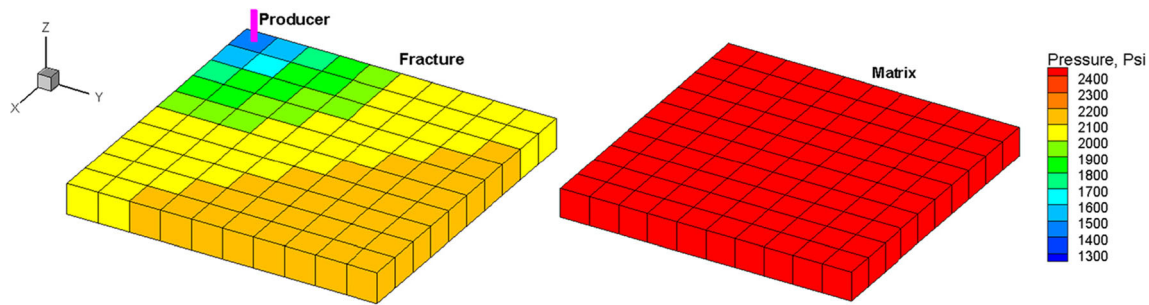


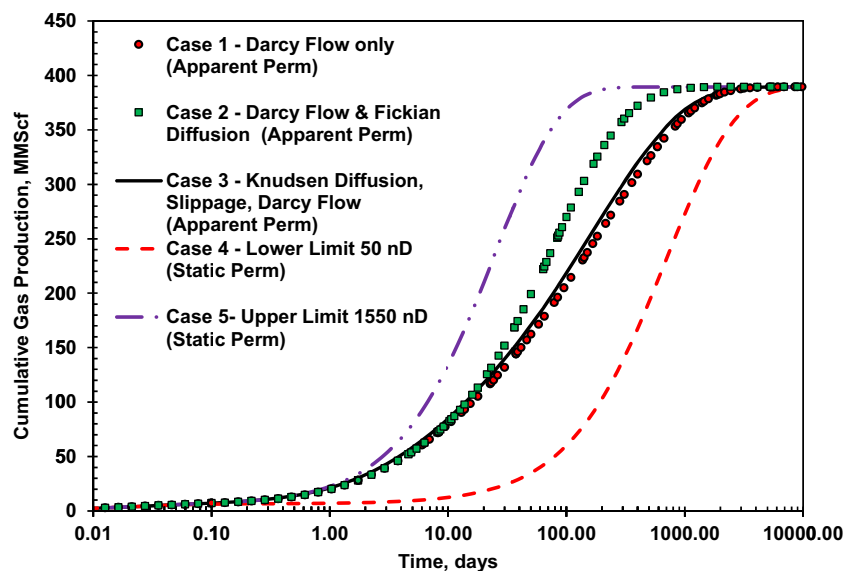
**Fig. 30** Dual-porosity model used for validation of variable permeability, *left map*: fracture; *right map*: matrix

Javadpour's model is obtained with implicit consideration of transient fluid transfer between matrix and fracture at the early production period. The resultant dynamic apparent permeability ratio curves are plotted together in Fig. 29. In the figure, for the given reservoir information, the result of case 3 based on Javadpour's model is much lower than that of case 2 considering Darcy flow and Fickian diffusion for most of the period, but slightly higher than that of case 1 only considering Darcy flow, because based on Fig. 27 matrix permeability is only slightly enhanced in the pressure drainage window of production after considering Knudsen diffusion and slippage flow in matrix.

Ultimately, the above upscaled apparent permeability ratio curves are applied to the macro-scale dual-porosity model with hydraulic fractures, shown in Fig. 30. The model is based on a simple  $10 \times 10 \times 1$  system of matrix blocks surrounded by a hydraulic fracture system, with producer perforated in fracture system only, which makes good sense for a dual-porosity single permeability model here. To account for the transient fluid transfer between matrix and fractures, people propose different approaches.

A popular scheme is to use variational discretization fashions to increase resolution, such as classic MINC [34] and subdomain [17] to subdivide matrix, and even the application of adaptive mesh refinement (AMR) in fracture domain [28]. People also investigated methods to use analytical or semi-analytical methods to consider the complex interporosity transfer [27, 30]. For the workflow in this paper, with upscaled apparent permeabilities from the fine micro-scale model, transient fluid transfer is already implicitly incorporated in the upscaled dynamic curves and consistent results have been obtained between coarse models and fine models (Fig. 26). Therefore, in the following dual-porosity model, it should be sufficient to capture the transient fluid flow merely with the application the dynamic apparent permeability for matrix. Reservoir is produced with constrain of constant bottom hole pressure, and at the early production period pressure in the fractures decreases dramatically to the BHP level because of the high flow conductivity in the fractures system. Therefore, basically, fractures play the role of constant pressure boundary condition during most of the period of the pressure drainage in the matrix. Under such

**Fig. 31** Matrix pressures for macro-model showing effect of variable permeability



scenario, Mora [29] suggested to use a shape factor from Lim and Aziz [25], shown as Eq. 14.

$$\sigma = \pi^2 \left( \frac{1}{L_x^2} + \frac{1}{L_y^2} + \frac{1}{L_z^2} \right) \quad (14)$$

Results of five different simulations at the macro-scale are shown in Fig. 31. Here cases 1 to 3 are dual-porosity models with upscaled matrix apparent permeability corresponding to cases 1 to 3 in Fig. 29, and case 4 and case 5 are respectively dual-porosity models with static matrix permeabilities from the lower and upper limit matrix permeability in cases 1 to 3 in Fig. 29. In Fig. 31, cases 1 to 3 with enhanced variable matrix permeability fall between cases 4 and 5 with static matrix permeabilities and cases 4 and 5 here cannot accurately capture the transient flow because of the only usage of static permeability in coarse matrix cells; however, cases 1 to 3 did a good job on this because of their inheritance from refined micro-scale models. As expected, this figure shows consistent results with Fig. 29. Specifically, case 3 coupling Knudsen diffusion, slippage and Darcy flow in upscaled matrix apparent permeability does not make significant difference from case 1 considering Darcy flow only during the upscaling process, because it is already analyzed that those mechanisms does not play a significant role to enhance the matrix permeability for the specific reservoir condition here. On the other hand, here case 2 with Darcy flow and Fickian diffusion produces faster than cases 1 and 3, since essentially this case does show a good enhancement of matrix permeability through the previous evaluation in Fig. 29. The results prove that the micro-scale model with different flow mechanisms can be upscaled efficiently in this manner.

## 10 Conclusions

The following conclusions can be made based on the results of the study:

- This research proposes a micro-scale model with natural fractures and shale matrix subdivided into three random distributed continua with Darcy flow, Fickian diffusion, and desorption in kerogen being considered.
- With a considerable adsorbed gas weight percentage in shale matrix, gas desorption from kerogen provides more gas in place and sustains a much greater cumulative gas rate and slightly higher average matrix pressure; however, the gas drainage capacity (similar to productivity index) and the apparent permeability defined in this paper are not significantly affected.
- Fickian diffusion cannot be neglected and is crucial to produce gas in the nano-pores in the kerogen. It is fairly

effective to enhance the gas drainage capacity and the apparent permeability as well.

- Darcy flow, Fickian diffusion, and desorption occur sequentially in our model. The latter two mechanisms are strengthened at the later time or lower average pressure in the matrix bulk because Darcy flow and free gas release dominate the early period.
- The difference of the micro-scale model and conventional dual-porosity model with the same pore volume is significant: the former takes into account Fickian diffusion and desorption so that the system has higher production rates and the associated more rapid pressure drop.
- With a constant TOC content in shale, different random distributions of kerogen have a negligible difference in the global gas flow behavior from shale matrix bulk to the natural fractures. The pressure map within the matrix bulk is well-matched with the distribution of matrix grid blocks. Higher TOC content in the shale effectively increases gas in place due to more adsorbed gas and free gas and also magnifies the role of diffusion in kerogen.
- The relationship of apparent matrix permeability ratio with pressure is independent of desorption effect, matrix size, and fracture permeability. This also implies the matrix apparent permeability ratio is an average property for the matrix bulk and captures the transient transfer and thus provides reliable base for upscaling the micro-scale model.
- Through introducing a coefficient considering the interaction between matrix and fracture to calculate matrix apparent permeability ratio, the transient flow, flow mechanism complexity (Darcy flow and diffusion), as well as the heterogeneity in the matrix can be accurately captured.
- Finally, the micro-scale model can be effectively upscaled through the variable matrix apparent permeability ratio.

**Acknowledgments** The authors wish to thank The Crisman Institute at Texas A&M University for funding this research project.

## Nomenclature

AGWP,	adsorbed gas weight percentage (wt%);
$\sum A_{mf}$ ,	total contact area between the matrix bulk and the fracture system (m <sup>2</sup> );
$C_g$ ,	gas compressibility (1/Pa);
$D_f$ ,	Fickian diffusion coefficient (m <sup>2</sup> /s);
$D_k$ ,	Knudsen diffusion coefficient (m <sup>2</sup> /s);
$D_m$ ,	effective Knudsen diffusion coefficient for porous medium (m <sup>2</sup> /s);
$d_{mf}$ ,	nodal distance between the matrix bulk and the fracture system (m);

$F$ ,	gas slippage factor (dimensionless);	$\rho_g$ ,	gas density at reservoir conditions ( $\text{kg/m}^3$ );
$f$ ,	fraction of molecules striking pore wall and diffusely reflected (value used here is 0.8 [22]);	$\rho_{g\text{-std}}$ ,	gas density at standard temperature and pressure (273.15 K and 101.325 Pa) ( $\text{kg/m}^3$ );
Frac,	natural fracture grid;	$\bar{\rho}_{\text{mf}}$ ,	average gas density in the micro model (fracture and matrix) ( $\text{kg/m}^3$ );
$g$ ,	the gravitational acceleration vector ( $\text{m}^2/\text{s}$ );	$\rho_s$ ,	the skeleton density of the porous media ( $\text{kg/m}^3$ );
Inorg	inorganic matrix grid;	$\sigma$ ,	shape factor ( $1/\text{m}^2$ );
$J_{\text{gD}}$ ,	gas drainage capacity ( $\text{kg/s/MPa}$ );	$\tau$ ,	tortuosity (dimensionless, value used here is 65 [40]);
$K$ ,	media permeability ( $\text{m}^2$ );	$\omega$ ,	coefficient considering the interaction between matrix and fracture
$K_{\text{app}}$ ,	apparent permeability within matrix ( $\text{m}^2$ or nanodarcy);		
$K_{\text{Ja}}$ ,	apparent permeability considering Knudsen diffusion, slippage, and Darcy flow based on Javadpour's model [22] ( $\text{m}^2$ or nanodarcy);		
$K_{\text{mapp}}$ ,	matrix apparent permeability totally excluding the influence of fracture, $\text{m}^2$ or nanodarcy;		
$K_f$ ,	fracture permeability ( $\text{m}^2$ );		
$L_x, L_y, L_z$ ,	matrix block size in $x$ -, $y$ -, and $z$ -direction (m);		
$M_g$ ,	gas molar weight (g/mol);		
Micro,	organic grid with micropores;		
$N_i$ ,	grid number of $i$ type matrix (where $i$ is Nano, Micro, or Inorg);		
Nano,	organic grid with nanopores;		
$P$ ,	pressure (Pa);		
$P_f$ ,	constant pressure in fracture system (Pa);		
$P_L$ ,	Langmuir pressure (Pa);		
$\bar{P}$ ,	average reservoir pressure (Pa);		
$\bar{P}_m$ ,	average pressure within the matrix bulk (inorganic grids and organic grids in total) (Pa);		
$q_a$ ,	the mass of gas adsorbed on unit volume of media ( $\text{kg/m}^3$ );		
$q_{\text{mf}}$ ,	total rate flowing from matrix system into fracture system ( $\text{kg/s}$ );		
$R$ ,	universal gas constant ( $8.314 \text{ J/K/mol}$ );		
$r$ ,	pore radii of porous media (m);		
$T$ ,	temperature (K);		
$t$ ,	time (s);		
TOC,	weight percentage of total organic carbon (wt%);		
$V$ ,	medium bulk volume ( $\text{m}^3$ );		
$V_L$ ,	Langmuir volume ( $\text{m}^3/\text{kg}$ );		
$W_f$ ,	weight of fracture system for harmonic average;		
$W_m$ ,	weight of matrix for harmonic average;		
$V_{\text{std}}$ ,	the molar volume of gas at standard temperature and pressure (273.15 K and 101.325 Pa);		
$z$ ,	distance in the gravitational direction (m);		
$Z$ ,	real gas deviation factor;		
$\delta$ ,	fracture aperture (m);		
$\phi$ ,	the porosity of the porous media (fraction);		
$\mu_g$ ,	gas viscosity (Pa s);		
$\bar{\mu}_{\text{mf}}$ ,	average gas viscosity in the micro model (fracture and matrix) (Pa S);		
$\rho$ ,	density ( $\text{kg/m}^3$ );		

## References

1. Aguilera, R.: Incorporating capillary pressure, pore throat aperture radii, height above free-water table, and Winland  $r_{35}$  values on Pickett plots. AAPG Bull. **86**(4), 605–624 (2002)
2. Alfi, M., Yan, B., Cao, Y., et al.: Three-phase flow simulation in ultra-low permeability organic shale via a multiple permeability approach. Soc. Pet. Eng. (2014). doi:[10.15530/urtec-2014-1895733](https://doi.org/10.15530/urtec-2014-1895733)
3. Ambrose, R.J., Hartman, R.C., Diaz-Campos, M., et al.: Shale gas-in-place calculations part I: new pore-scale considerations. (2012). doi:[10.2118/131772-PA](https://doi.org/10.2118/131772-PA)
4. Andrade, J., Civan, F., Devegowda, D., et al.: Design and examination of requirements for a rigorous shale-gas reservoir simulator compared to current shale-gas simulator. Paper presented at the North American Unconventional Gas Conference and Exhibition. The Woodlands, Society of Petroleum Engineers SPE-144401-MS. (2011). doi:[10.2118/144401-ms](https://doi.org/10.2118/144401-ms)
5. Beskok, A., Karniadakis, G.E.: A model for flows in channels, pipes, and ducts at micro and nano scales. Microscale Thermophys. Eng. **3**(1), 43–77 (1999)
6. Civan, F.: Effective correlation of apparent gas permeability in tight porous media. Transp. Porous Media **82**(2), 375–384 (2010). doi:[10.1007/s11242-009-9432-z](https://doi.org/10.1007/s11242-009-9432-z)
7. Civan, F., Rai, C., Sondergeld, C.: Shale-gas permeability and diffusivity inferred by improved formulation of relevant retention and transport mechanisms. Transp. Porous Media **86**(3), 925–944 (2011). doi:[10.1007/s11242-010-9665-x](https://doi.org/10.1007/s11242-010-9665-x)
8. Clarkson, C.R., Ertekin, T.: A new model for shale gas matrix flow using the dynamic-slippage concept. Paper presented at the AAPG Hedberg Conference, Austin, Texas (2010)
9. Cui, X., Bustin, A.M.M., Bustin, R.M.: Measurements of gas permeability and diffusivity of tight reservoir rocks: different approaches and their applications. Geofluids **9**(3), 208–223 (2009). doi:[10.1111/j.1468-8123.2009.00244.x](https://doi.org/10.1111/j.1468-8123.2009.00244.x)
10. Curtis, M.E., Ambrose, R.J., Sondergeld, C.H.: Structural characterization of gas shales on the micro- and nano-scales. Paper presented at the Canadian Unconventional Resources and International Petroleum Conference, Calgary, Alberta, Canada. Society of Petroleum Engineers SPE-137693-MS. (2010). doi:[10.2118/137693-ms](https://doi.org/10.2118/137693-ms)
11. Curtis, M.E., Sondergeld, C.H., Ambrose, R.J., et al.: Microstructural investigation of gas shales in two and three dimensions using nanometer-scale resolution imaging. AAPG Bull. **96**(4), 665–677 (2012). doi:[10.1306/08151110188](https://doi.org/10.1306/08151110188)
12. Ding, D.Y., Langouët, H., Jeannin, L.: Simulation of fracturing-induced formation damage and gas production from fractured wells in tight gas reservoirs. (2013). doi:[10.2118/153255-PA](https://doi.org/10.2118/153255-PA)

13. Ding, D.Y., Wu, Y.S., Jeannin, L.: Efficient simulation of hydraulic fractured wells in unconventional reservoirs. *J. Pet. Sci. Eng.* **122**, 631–642 (2014). doi:[10.1016/j.petrol.2014.09.005](https://doi.org/10.1016/j.petrol.2014.09.005)
14. Ertekin, T., King, G.A., Schwerer, F.C.: Dynamic gas slippage: a unique dual-mechanism approach to the flow of gas in tight formations. *SPE Form. Eval.* **1**(1), 43–52 (1986). doi:[10.2118/12045-pa](https://doi.org/10.2118/12045-pa)
15. Freeman, C., Moridis, G.J., Michael, G.E., et al.: Measurement, modeling, and diagnostics of flowing gas composition changes in shale gas wells. Paper presented at the SPE Latin America and Caribbean Petroleum Engineering Conference, Mexico City, Mexico. Society of Petroleum Engineers SPE-153391-MS. (2012). doi:[10.2118/153391-ms](https://doi.org/10.2118/153391-ms)
16. Furui, K., Zhu, D., Hill, A.D.: A rigorous formation damage skin factor and reservoir inflow model for a horizontal well. Society of Petroleum Engineers. (2002). doi:[10.2118/74698-MS](https://doi.org/10.2118/74698-MS)
17. Gilman, J.R.: An efficient finite-difference method for simulating phase segregation in the matrix blocks in double-porosity reservoirs. *SPE Reserv. Eng.* **1**(4), 403–413 (1986). doi:[10.2118/12271-pa](https://doi.org/10.2118/12271-pa)
18. Hill, D.G., Nelson, C.R.: Gas productive fractured shales—an overview and update. *Gas TIPS*, pp. 4–13 (2000)
19. Hoteit, H., Firoozabadi, A.: Numerical modeling of diffusion in fractured media for gas injection and recycling schemes. Paper presented at the SPE Annual Technical Conference and Exhibition, San Antonio, Texas, USA. Society of Petroleum Engineers SPE-103292-MS. (2006). doi:[10.2118/103292-ms](https://doi.org/10.2118/103292-ms)
20. Hudson, J.D., Civan, F., Michel, G., et al.: Modeling multiple-porosity transport in gas-bearing shale formations. Paper presented at the SPE Latin America and Caribbean Petroleum Engineering Conference, Mexico City, Mexico. Society of Petroleum Engineers SPE-153535-MS. (2012). doi:[10.2118/153535-ms](https://doi.org/10.2118/153535-ms)
21. Jarvie, D.: Evaluation of hydrocarbon generation and storage in Barnett Shale, Fort Worth Basin, Texas. Paper presented at the Petroleum Technology Transfer Council. The University of Texas at Austin, Bureau of Economic Geology (2004)
22. Javadpour, F.: Nanopores and apparent permeability of gas flow in mudrocks (shales and siltstone). *J. Can. Pet. Technol.* **48**(08), 16–21 (2009)
23. Javadpour, F., Fisher, D., Unsworth, M.: Nanoscale gas flow in shale gas sediments. *J. Can. Pet. Technol.* **46**(10) (2007). doi:[10.2118/07-10-06](https://doi.org/10.2118/07-10-06)
24. King, G.E.: Thirty years of gas shale fracturing: What have we learned? Paper presented at the SPE annual technical conference and exhibition, Florence, Italy. Society of Petroleum Engineers SPE-133456-MS (2010). doi:[10.2118/133456-ms](https://doi.org/10.2118/133456-ms)
25. Lim, K.T., Aziz, K.: Matrix-fracture transfer shape factors for dual-porosity simulators. *J. Pet. Sci. Eng.* **13**(3–4), 169–178 (1995). doi:[10.1016/0920-4105\(95\)00010-F](https://doi.org/10.1016/0920-4105(95)00010-F)
26. Loucks, R.G., Reed, R.M., Ruppel, S.C., et al.: Spectrum of pore types and networks in mudrocks and a descriptive classification for matrix-related mudrock pores. *AAPG Bull.* **96**(6), 1071–1098 (2012). doi:[10.1306/08171111061](https://doi.org/10.1306/08171111061)
27. Lu, H.: Investigation of recovery mechanisms in fractured reservoirs. PhD Dissertation, Imperial College (2007)
28. Luo, H.-S., Wang, X.-H., Quintard, M.: Adaptive mesh refinement for one-dimensional three-phase flows in heterogeneous fractured porous media. *Numerical Heat Transfer, Part B: Fundamentals* **54**(6), 476–498 (2008). doi:[10.1080/10407790802424105](https://doi.org/10.1080/10407790802424105)
29. Mora, C.A.: Comparison of Computation methods for CBM production performance. Master of Science Thesis, Texas A&M University (2007)
30. Nøttinger, B.: A quasi steady state method for solving transient Darcy flow in complex 3d fractured networks accounting for matrix to fracture flow. *J. Comput. Phys.* **283**, 205–223 (2015). doi:[10.1016/j.jcp.2014.11.038](https://doi.org/10.1016/j.jcp.2014.11.038)
31. Odusina, E.O., Sondergeld, C.H., Rai, C.S.: An NMR study of shale wettability. Paper presented at the Canadian Unconventional Resources Conference, Alberta, Canada. Society of Petroleum Engineers SPE-147371-MS. (2011). doi:[10.2118/147371-ms](https://doi.org/10.2118/147371-ms)
32. Passey, Q.R., Bohacs, K., Esch, W.L., et al.: From oil-prone source rock to gas-producing shale reservoir—geologic and petrophysical characterization of unconventional shale-gas reservoirs. Paper presented at the International Oil and Gas Conference and Exhibition in China, Beijing, China. Society of Petroleum Engineers SPE-131350-MS. (2010). doi:[10.2118/131350-ms](https://doi.org/10.2118/131350-ms)
33. Pruess, K.: GMINC—a mesh generator for flow simulations in fractured reservoirs (1982)
34. Pruess, K.: A practical method for modeling fluid and heat flow in fractured porous media. *Soc. Pet. Eng. J.* **25**(1), 14–26 (1985). doi:[10.2118/10509-pa](https://doi.org/10.2118/10509-pa)
35. Shabro, V., Torres-Verdin, C., Javadpour, F.: Numerical simulation of shale-gas production: from pore-scale modeling of slip-flow, Knudsen diffusion, and Langmuir desorption to reservoir modeling of compressible fluid. Paper presented at the North American Unconventional Gas Conference and Exhibition, The Woodlands, Texas, USA. Society of Petroleum Engineers SPE-144355-MS. (2011). doi:[10.2118/144355-ms](https://doi.org/10.2118/144355-ms)
36. Shabro, V., Torres-Verdin, C., Sepehrmoori, K.: Forecasting gas production in organic shale with the combined numerical simulation of gas diffusion in kerogen, Langmuir desorption from kerogen surfaces, and advection in nanopores. Paper presented at the SPE Annual Technical Conference and Exhibition, San Antonio, Texas, USA. Society of Petroleum Engineers SPE-159250-MS. (2012). doi:[10.2118/159250-ms](https://doi.org/10.2118/159250-ms)
37. Sigal, R.: A note on the intrinsic porosity of organic material in shale gas reservoir rocks. <http://shale.ou.edu/Home/Publication> (2011)
38. Sun, J., Hu, K., Wong, J., et al.: Investigating the effect of improved fracture conductivity on production performance of hydraulic fractured wells through field case studies and numerical simulations. Society of Petroleum Engineers. (2014). doi:[10.2118/169866-MS](https://doi.org/10.2118/169866-MS)
39. Sun, J., Schechter, D.S.: Optimization-based unstructured meshing algorithms for simulation of hydraulically and naturally fractured reservoirs with variable distribution of fracture aperture, spacing, length and strike. Society of Petroleum Engineers. (2014). doi:[10.2118/170703-MS](https://doi.org/10.2118/170703-MS)
40. Swami, V., Clarkson, C.R., Settari, A.: Non-Darcy flow in shale nanopores: do we have a final answer? Society of Petroleum Engineers. (2012). doi:[10.2118/162665-MS](https://doi.org/10.2118/162665-MS)
41. Wang, F.P., Reed, R.M.: Pore networks and fluid flow in gas shales. Paper presented at the SPE Annual Technical Conference and Exhibition, New Orleans, Louisiana. Society of Petroleum Engineers SPE-124253-MS. (2009). doi:[10.2118/124253-ms](https://doi.org/10.2118/124253-ms)
42. Wu, Y.-S., Li, J., Ding, D., et al.: A generalized framework model for the simulation of gas production in unconventional gas reservoirs. (2014). doi:[10.2118/163609-PA](https://doi.org/10.2118/163609-PA)
43. Zhang, J., Kamenov, A., Hill, A.D., et al.: Laboratory measurement of hydraulic-fracture conductivities in the Barnett Shale. (2014). doi:[10.2118/163839-PA](https://doi.org/10.2118/163839-PA)
44. Zhang, J., Ouyang, L., Hill, A.D., et al.: Experimental and numerical studies of reduced fracture conductivity due to proppant embedment in shale reservoirs. Society of Petroleum Engineers. (2014). doi:[10.2118/170775-MS](https://doi.org/10.2118/170775-MS)
45. Zhang, J., Zhu, D., Hill, A.D.: Water-induced fracture conductivity damage in shale formations. Society of Petroleum Engineers. (2015). doi:[10.2118/173346-MS](https://doi.org/10.2118/173346-MS)
46. Ziarani, A., Aguilera, R.: Knudsen's permeability correction for tight porous media. *Transp. Porous Media* **91**(1), 239–260 (2012). doi:[10.1007/s11242-011-9842-6](https://doi.org/10.1007/s11242-011-9842-6)